Melt Pond Variability in the Southern Patagonian Icefield and Influence of the Southern Annular Mode

Lauri Stevens, S4916093
University of Groningen, Campus Fryslan
Capstone Bachelor Thesis
Dr. Sarah C. Feron
12 July 2024

Melt ponds play an important role in glacial surface melt, and are thus important to look into considering projected future sea level rise. As the largest ice mass in the Southern Hemisphere, the Southern Patagonian Icefield (SPI) is a main contributor. To better predict the future, understanding variability in melting and what climatic factors drive it is crucial. However, this is a topic that has not been studied extensively. I used Sentinel-2 satellite imagery of glaciers in the Southern Patagonian Icefield over a period from December 2018 to December 2023 and applied a Random Forest (RF) algorithm to classify melt ponds. I found a large range of variability in melt pond area both comparing between glaciers (with mean relative areas ranging between 0.3% on Pio XI to 1.9% on Upsala), and over time (0%-3.5% relative area). Any seasonality in this area appeared unclear. I found the Southern Annular Mode (SAM) to not have a significant effect on pond area.

Table of Contents

Introduction

Globally, glacier mass loss has been a major factor causing sea level rise, and thus an increasing concern (Cazenave & Llovel, 2010). In recent decades this ice loss has been increasing (Bravo, Bozkurt, et al., 2021). Meltwater from land ice is increasingly affecting sea level rise – and with a total contribution of 3.3 mm yr^{-1}, South Andean glaciers are some of the highest contributors. Through climate change, temperatures are projected to increase. Subsequently, this ice loss and corresponding sea level rise contribution is expected to increase as well, and can mostly be attributed to increasing surface melt (Bravo, Bozkurt, et al., 2021).

Not considering Antarctica, the Southern Patagonian Icefield (SPI) is the largest ice mass in the Southern Hemisphere (Schaefer et al., 2015; Casassa et al., 2002). It is located in the Andes, on the border between Chile and Argentina, and has an area of 13,000 km^2 covering 48 major glaciers. Two of those glaciers terminate on land; the rest calve into freshwater lakes and fjords. With a total area of 1265 km^2, Pio XI (also called the Brüggen Glacier) is the largest glacier of the SPI (Casassa et al., 2002; ESA, 2016).

Dussaillant et al. (2019), who studied glacier mass loss in 2000-2019, found the highest mass loss of the Andes region in South Patagonia. Most of the SPI glaciers have been retreating (though contrary to this trend, Pío XI has both advanced and thickened during this period) (Carrivick et al., 2016; Hata & Sugiyama, 2021; Schaefer et al., 2015).

Therefore, it is important to study this melting in more detail: understanding the recent past and the present glacial melting will ensure better prediction of what could happen in the future. This is a topic that is already being researched quite extensively. For this research, understanding the interannual variability of surface melting is crucial. This is for multiple reasons: quantify the signal-to-noise ratio in climate trends, assess the performance of climate models, and to improve predictions (Donat-Magnin et al., 2020). The interannual variability in glacial surface melt and its possible climatic drivers, especially in the context of the SPI, present a gap in current research and are crucial to look into more (Carrasco-Escaff et al., 2023).

More concretely, this study will look into the Southern Annular Mode (SAM) as possible drivers of glacial melt. ‘Glacial melt’ here is defined as supraglacial lakes (SGLs), or in other words, melt ponds. This is both because glacier melt area is characterised by SGLs, and because SGLs themselves influence further melting. They do so in two ways: they both lower the albedo, and affect ice flow velocity by reducing basal friction (i.e. friction between the bottom layer of the glacier and the land surface below; this speeds up the glacier) (Hochreuther et al., 2021).

The aims of this study are to study interannual variability in the area of SPI melt ponds over a period of 5 years (December 2018 – December 2023; the period in which satellite (Sentinel-2 L2A) data was available), to look into possible differences in these area trends between SPI glaciers, and to study the effects of the SAM on this interannual variability.

Summarised, the research question of this study is: “How can the SPI glaciers’ melt ponds be characterised, and what influence does the SAM have over their occurrence?”

Because of this study’s requirements regarding temporal and spatial resolution, satellite-based remote sensing will be used. Two methods of classifying melt pond area will be

tested and compared (a band ratio – threshold based method and a random forest (RF) model as a supervised machine learning (ML) method).

First, in the following literature review section, more detail will be provided on the Southern Patagonian Icefield and its glaciers, and previous research on glacial melt ponds and the above mentioned climate modes will be summarised. Subsequently, the data products and methodology of this study will be discussed. Following, the results will be presented and discussed, and conclusions will be drawn.

Literature Review

The Southern Patagonian Icefield

Geography and Climate

As mentioned before, the SPI is the largest ice mass in the Southern Hemisphere barring Antarctica: it has an area of 13,000 km^2, and a volume of 4,300 km^3 (Carrivick et al., 2016; Foresta et al., 2018). See Figure 1 for its location, indicated in purple: the ice field stretches between 48°20′S and 51°30′S (López et al., 2010). Its average altitude is 1355 metres above sea level (Willis et al., 2012). Its highest peak is Cerro Fitz Roy at 3405 metres above sea level (López et al., 2010).

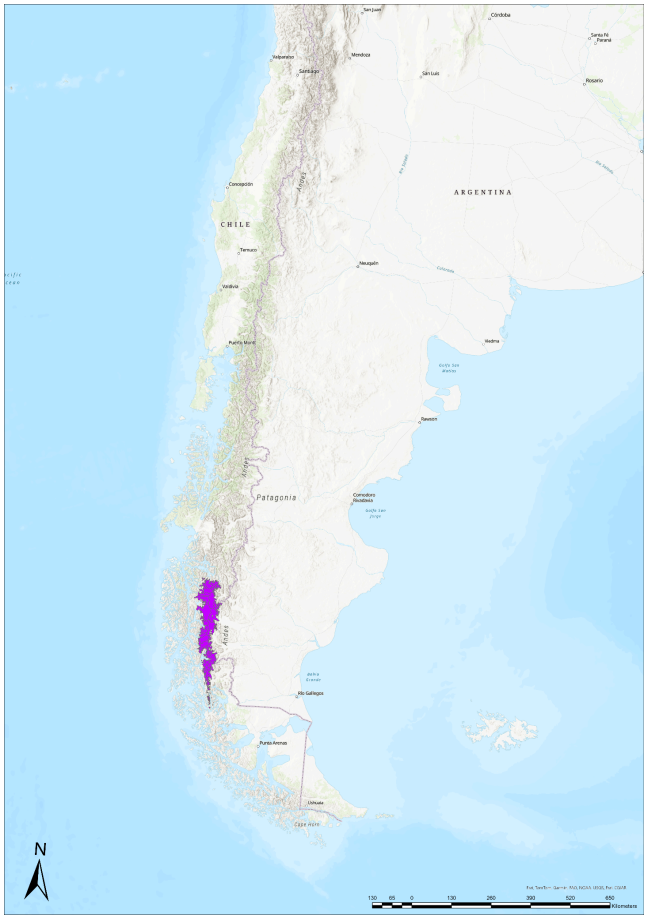

Figure 1: Location of the SPI (purple) Map based on glacier delineations adapted from Davies et al. (2020) (ArcGIS Pro 3.3.0)

The majority of the glaciers on the SPI's eastern side terminate in lakes, while many on the western side calve into seawater (Willis et al., 2012). Generally, glaciers in the north of the ice field are bigger than the ones in the southern part (López et al., 2010). Pio XI, with an area of 1265 km^2, is the largest glacier in not only the SPI but in all of South America (López et al., 2010). This study specifically will focus on seven different SPI glaciers: Pio XI, Perito Moreno, Chico, HPS12, Upsala, Occidental, Jorge Montt, and O'Higgins. These were chosen for their variety in location, differing areas, and differences in historical retreating/advancing behaviour. For the locations of the glaciers, see Figure 2. All glaciers' areas and their general East/West locations are listed in Table 1 (López et al, 2010).

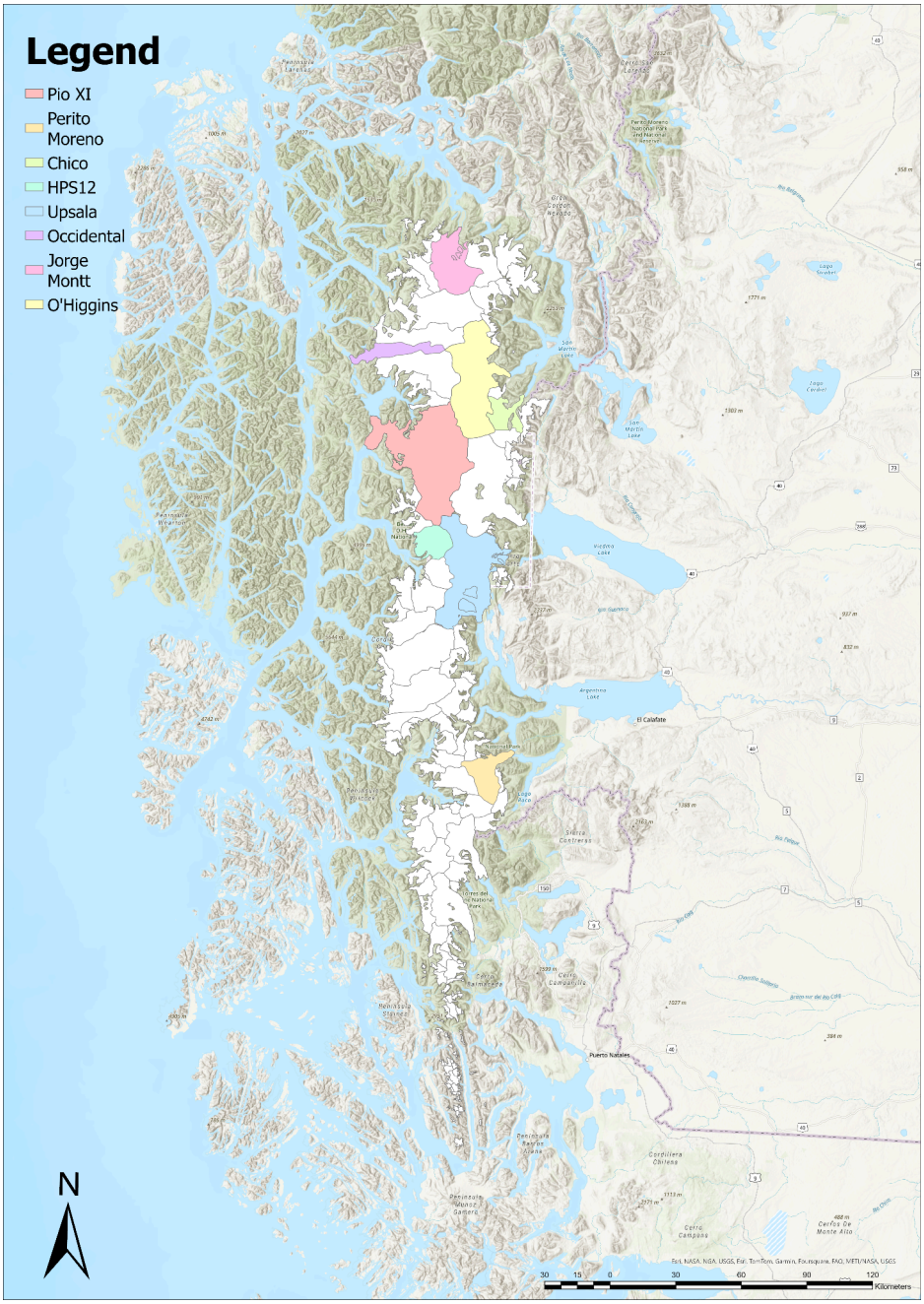

Figure 2: Locations of studied SPI glaciers
Map based on glacier delineations adapted from Davies et al. (2020) (ArcGIS Pro 3.3.0)

Table 1: Glacier areas

Glacier	**Area (km^2)**	**Location (East/West)**
Pio XI	1292.2	East
Perito Moreno	265.0	West
Chico	166.5	West
HPS12	178.9	East
Upsala	900.5	West
Occidental	448.2	East
Jorge Montt	403.0	West
O'Higgins	785.4	East

Note. Adapted from "A regional view of fluctuations in glacier length in southern South America," by P. López et al., 2010, *Global and Planetary Change*, *71*(1–2), 85–108. https://doi.org/10.1016/j.gloplacha.2009.12.009.

The SPI is fed by westerly winds (see Figure 3) that flow over the Pacific Ocean and collide with the mountains, which are shaped mainly north to south: this induces precipitation following the so-called orographic effect. In the western (windward) side, air collides with the mountains, rises, becomes saturated, and precipitation occurs. The eastern (leeward) side encounters air subsidence, and thus receives less precipitation than on the windward side (Bravo, Ross, et al., 2021). The SPI region as a whole receives between 2 and 11 metres of water equivalent per year (Rignot et al., 2003). This, though, is clearly not spatially homogeneous. The two sides of the SPI have distinct and different meteorological conditions.

The clearest impact of this orographic effect-induced difference is that it ensures cloud cover is higher on the western side of the SPI compared to the east (Bravo, Ross, et al., 2021). As a result, the east receives a higher magnitude of incoming shortwave radiation than the west (Bravo, Ross, et al., 2021; Schaefer et al., 2015). The resulting difference in lapse rates between the western and eastern glaciers can result in unequal rates of surface ablation (Bravo et al., 2019; Bravo, Ross, et al., 2021). Because surface ablation is dominated by melt, and melt is strongly sensitive to surface air temperature, these differences in lapse rate and resulting differences in temperature could result in spatially varying magnitudes of glacier melting (Bravo et al., 2019; Malz et al., 2018). Bravo et al. used data from 5 Automatic Weather Stations (AWS; data from October 2015 to June 2016) in the north of the SPI, and found that at comparable elevations, off-glacier temperatures in the east were higher than in the west, whereas on-glacier temperatures and computed ablation were higher in the west than in the east (2019). They found that the magnitude of the incoming shortwave radiation was higher in the east than in the west,

while the magnitude of the incoming longwave radiation was higher in the west than in the east – this can be attributed to the cloud cover differences.

It has also been suggested that the onset of the melt season could be earlier in the east than in the west. Overall, it is clear that the SPI has an important spatial variability in meteorology and resulting ablation, and should thus not be treated as a homogenous area (Bravo et al., 2019).

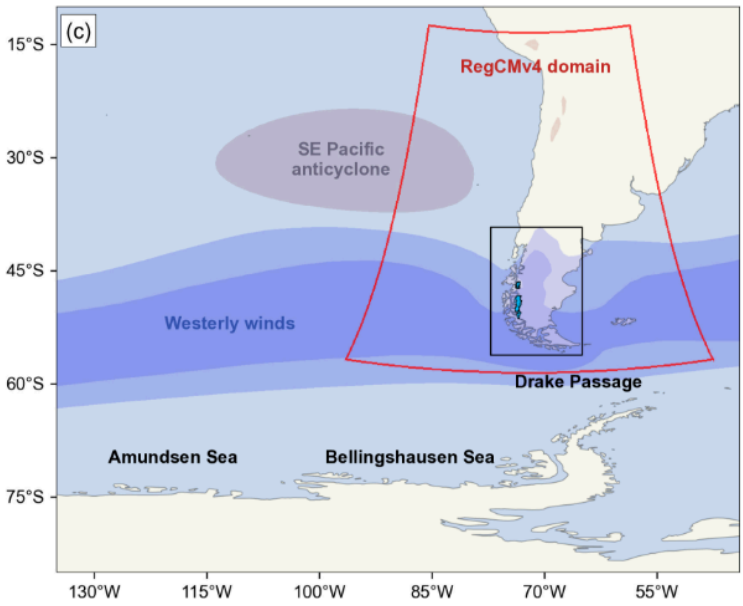

Figure 3: Main circulation near Patagonian icefields

Note. From "Climatic control of the surface mass balance of the Patagonian Icefields," by T. Carrasco-Escaff et al., 2018, *the Cryosphere*, *17*(3), 1127–1149. https://doi.org/10.5194/tc-17-1127-2023. CC-BY.

Historical Melting Behaviour

Many previous studies have made attempts at quantifying melting and mass loss in the SPI. The following section is a non-comprehensive overview of some of those studies, intended to provide an overview of the SPI's melting over the past decades.

Since at least the 1950s, most of the SPI's glaciers have been retreating and thinning (Braun et al., 2019; Dussaillant et al., 2019; López et al., 2010; Rignot et al., 2003; Willis et al., 2012). This melting has been accelerating over time (Foresta et al., 2018; Willis et al., 2012). Willis et al found a mass loss of -20.0 ± 1.2 Gt a^{-1} between 2000-2012: this is about 150% of the Northern Patagonian Icefield (NPI) and SPI combined melting reported during 1968/75 to 2000 (Rignot et al., 2003; Willis et al., 2012). The only glacier that has been advancing instead of retreating is Pio XI (Hata & Sugiyama, 2021; López et al., 2010; Rignot et al., 2003). Findings by Hata and Sugiyama, who studied Pio XI melting specifically, show that during their period of study (2000-2018) Pio XI both thickened and advanced, and overall saw a positive mass balance of 0.48 ± 0.03 Gt a^{-1} (2021).

Foresta et al. looked into SPI ice loss using CryoSat-2 swath radar altimetry (i.e. an ESA mission targeted at monitoring ice sheet elevation and elevation change) between April 2011 and March 2017 (2018). Figure 4 displays their resulting elevation change map. As can be seen, rapid thinning (of 2 Gt a^{-1} or more) has been occurring in the north of the SPI, while many glaciers in the south/southwest are almost balanced. A notable exception is (again) Pio XI, which has been thickening up until 1500 metres altitude. In total in this period, the SPI has seen a mass loss of -14.50 ± 1.60 Gt a^{-1}. With a mass loss of -2.68 ± 0.40 Gt a^{-1}, Upsala Glacier was the largest contributor. (Pio XI was the only glacier with a positive mass balance (0.67 ± 0.29 Gt a^{-1})). They affirm the finding that over time glacier mass loss has been increasing. In the period between 2011-2017, the NPI and the SPI combined have seen an increase in mass loss of 24% compared to 2000–2012/14, and even 42% compared to 1975–2000 (Foresta et al., 2018).

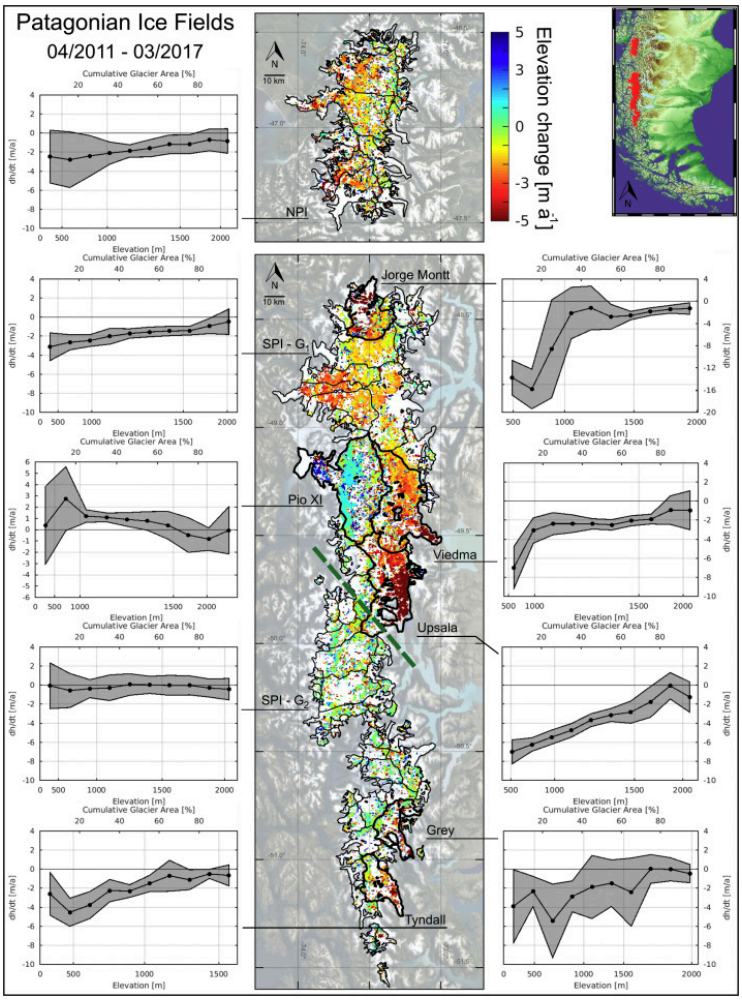

Figure 4: Patagonian Ice Field Elevation Change

Note. From "Heterogeneous and rapid ice loss over the Patagonian Ice Fields revealed by CryoSat-2 swath radar altimetry," by L. Foresta et al., 2018, *Remote Sensing of Environment*, *211*, 441–455. https://doi.org/10.1016/j.rse.2018.03.041. CC-BY.

Climate Modes

The strength of the westerly winds is an important control on Patagonian climate (Carrasco-Escaff et al., 2023; Garreaud et al., 2013). Garreaud et al. have found correlations between zonal wind and temperature and zonal wind in precipitation in the region (2013). Thus, factors such as climate modes that have an influence over the strength of these westerlies impact the climate as well (Carrasco-Escaff et al., 2023).

Climate modes are important drivers of climate variability, and could influence glacier melting in different ways: for example, they can have effects on precipitation or surface air temperature (SAT). Since few prior studies have investigated associations between climate modes and SPI glaciers' melt ponds directly, mainly assumptions can be made. Below, some of these modes and their climatic effects will be discussed. At the end of each subsection, hypotheses will be made on what effects these mode-induced climate effects in turn could have on SPI glacier melting.

El Niño–Southern Oscillation

The El Niño–Southern Oscillation (ENSO) is the Earth's main driver of interannual climate variability, as well as the main mode of ocean and atmospheric variability in the tropical Pacific (Carrasco-Escaff et al., 2023; Donat-Magnin et al., 2020). At the seasonal to interannual timescale, it is the strongest driver of climate variability in Southern America (Donat-Magnin et al., 2020; Loikith et al., 2017). Previous studies looking into the relationship between temperature and ENSO have found that in South America warm ENSO phase events are associated with above average temperatures, while cool phase events are associated with below average temperatures (Loikith et al., 2017). A relationship between ENSO warm phase events and extreme warm temperatures has been found as well. Loikith et al. studied the association between ENSO (quantified using the MEI distribution) and extreme high and extreme low (T90 and T10) temperatures in South America in both summer and winter (2017). Whereas they found significant relationships between ENSO+ and extreme high temperatures and ENSO- and extreme low temperatures in the northern half of the continent, (mainly in summer, but in winter as well) there was no clear association to be seen in the area of the SPI.

In addition, circulation anomalies can influence South American precipitation (Carrasco-Escaff et al., 2023). In western Patagonia, warm ENSO (i.e. El Niño) events have been linked to a decrease in precipitation, while the opposite effect was seen during La Niña (cold) events. However, "the net effect of ENSO on the Patagonian climate seems to depend on the specifics of each ENSO event" (Carrasco-Escaff et al., 2023).

Thus, ENSO most likely does not have a (significant) influence over the SPI glaciers' variability in melting behaviour.

Atlantic Niño

The Atlantic Niño (ANINO) refers to sea surface temperature (SST) variability in the Atlantic Ocean (Loikith et al., 2017). This mode has been shown to influence Southern American climate mainly by influencing the location of the Intertropical Convergence Zone (ITCZ). Loikith et al. found a relatively weak though significant positive association between ANINO+ and summer extreme high temperatures over the southern tip of South America where the SPI is located (2017). Additionally, they found a stronger and significant association between ANINO- and extreme low summer temperatures. This could mean that ANINO has an indirect effect on melting: there could be an association between ANINO+ and increased summer melting, and between ANINO- and decreased summer melt pond area.

Pacific Decadal Oscillation

The Pacific Decadal Oscillation (PDO) is defined based on monthly variability in sea surface temperature (SST) (Loikith et al., 2017). Its temporal scale of variability is longer than that of ENSO. Generally, it is seen to have the same climatic influence over South America as ENSO, but with a lower (approximately half the) magnitude of influence. Additionally, the PDO and ENSO have been suggested to modulate each other: meaning, when both are in phase they reinforce each other, while when they are in opposing phases their influences counteract each other (Loikith et al., 2017). Evidence suggests that the PDO itself does not have a strong influence on temperature extremes in South America independently, but instead through its relationship with ENSO, and thus does not appear to have a strong (even indirect) effect on temperature extremes over the SPI. Because of this, the PDO most likely does not have an influence over SPI glaciers' melting either.

Southern Annular Mode

Contrary to ENSO, the ANINO, and the PDA, the Southern Annular Mode (SAM, also known as the Antarctic Oscillation (AAO)) is characterised by a higher frequency (Loikith et al., 2017). Additionally, it is not based on anomalies in SST, but rather based on anomalies in atmospheric circulation. When SAM is high (SAM+), the polar vortex is strong, confining cold Antarctic air in the South Pole. Conversely, SAM– means the polar vortex weakens, allowing cold Antarctic air to venture up to more northern areas.

South of the ~40° latitude, the SAM is positively correlated with temperature; i.e., warming is associated with SAM+ (Carrasco-Escaff et al., 2023; R. Garreaud et al., 2013; R. D. Garreaud et al., 2009; López et al., 2010). Though the SAM is active all year, it has been found to be strongest around November (i.e. the Southern Hemisphere spring). Loikith et al. looked into SAM effects on extreme temperatures in September–November (SON) and March–May (MAM) and found strong and significant effects in the SPI region in all cases (2017).

The SAM has been demonstrated to have an important effect in South American precipitation patterns as well: during SAM+ southern Patagonia experiences more precipitation

than average, while the opposite happens during SAM- (Aravena & Luckman, 2008; Carrasco-Escaff et al., 2023; R. D. Garreaud et al., 2009).

The above suggests that the SAM might have an influence on SPI glaciers' melting and melt pond area. A positive SAM could be associated with increased melt pond area, while a negative SAM might be correlated with lower area.

Materials and Methods

Because (Southern Patagonian) glaciers cover a large area, satellite-based remote sensing can best be used to study them. Conditions are so inhospitable, and area and time coverage requirements are so vast, that in situ measurement is often impossible. In particular, multispectral instruments (MSI) are useful, since SGLs can usually be determined using single bands, or band ratios (Hochreuther et al., 2021). Two key methodologies can be identified to map SGLs on Southern Patagonian glaciers: using a threshold-based method like a band ratio, and machine learning (ML) (Dell et al., 2021; Hochreuther et al., 2021). The former identifies melt ponds where pixels exceed a certain reflectance threshold (in often a band ratio) (Hochreuther et al., 2021). This approach can have a variable performance: given the similarities in spectral reflectance between melt ponds, blue ice, and shadows, the approach may work less well in some regions as compared to others (Dell et al., 2021). Additionally, the specific threshold set is region-specific, and might need to be changed if applied to different locations (Dell et al., 2021).

The latter is ML: typically, this method uses more information than the single-band or band ratio-based method outlined above. This is because ML methods themselves can determine which information is valuable in classifying. Though this method has drawbacks as well, mainly the fact that ML methods are much more computationally expensive, these can be overcome by cloud-based geospatial processing platforms like Google Earth Engine (GEE) (Dell et al., 2021). In this study, I test both a threshold-based band ratio method, and a ML (RF) one.

Materials

Google Earth Engine

This study will use data from the Google Earth Engine: this platform is free to use, and provides access to a number of core features (Tamiminia et al., 2020). To name a few, it provides access to petabytes of publicly available remote sensing images – these include MODIS, Landsat, and Sentinel 2 – and its computational infrastructure, importantly its built in code editor (available through a web-based Integrated Development Environment (IDE), allows for high-speed processing of high volumes of data. This IDE even provides the user with access to its own machine learning algorithms (Tamiminia et al., 2020). Both supervised (e.g. Naive Bayes, Random Forest, SVM) and unsupervised models are available (Google Earth Engine, n.d.-b, n.d.-c). I wrote a large part of this study's code in GEE's code editor, and made use of its built-in Random Forest model.

Sentinel-2

I used Sentinel-2 data to detect melt ponds. This was because of spatial and temporal resolution requirements. Since melt ponds are generally small, a high spatial resolution was necessary, which made using e.g. MODIS impossible. Additionally, a high temporal resolution was needed because of the cloudy nature of the area of interest. A two-week resolution like Landsat 8 would not have been possible to use, since the likelihood that at least one of two images a month was too cloudy to use was high.

Sentinel-2 is a project composed of two twin satellites: Sentinel-2A and Sentinel-2B (Google Earth Engine, n.d.-b, n.d.-c). It is coordinated by the Copernicus Programme, as part of the European Space Agency (ESA) project under the European Union's Earth Observation Programme (Phiri et al., 2020). Sentinel-2A was launched in 2015, and Sentinel-2B two years later. Both satellites carry multispectral imaging instruments (MSI) that are capable of recording reflectance data in 13 spectral bands. These bands include a red, green, and blue band in the visible spectrum, near infrared, and shortwave infrared (Phiri et al., 2020). The project provides its data in high spectral resolution (between 10-60 metres depending on the specific band) (Google Earth Engine, n.d.-a; Phiri et al., 2020). The Sentinel-2 satellites are in sun-synchronous orbit and cover the whole globe, such that the same location is revisited (at least) every five days (ESA, 2016; Phiri et al., 2020). All Sentinel-2 images are available free of charge through e.g. the Copernicus Open Access Hub, or through Google Earth Engine (Google Earth Engine, n.d.-a; Phiri et al., 2020).

Sentinel-2 data is available at different processing levels (Phiri et al., 2020). One of the most commonly used products is Level-2A. This product has gone through multiple processing stages (including e.g. geometric and atmospheric correction) to finally provide the so-called Surface/Bottom of Atmosphere Reflectance that this study will be making use of (Google Earth Engine, n.d.-a; Phiri et al., 2020).

Preprocessing

Preprocessing was required before starting any analysis. This was mainly to get the data in the right temporal resolution. Since, as mentioned earlier, Sentinel-2 images of Level 2A were used, there was no need for manual e.g. radiometric corrections. However, I filtered my images based on a cloud percentage (40%), and used an extra cloud filter based on the provided "QA60" bitmask (i.e., pixels with value 1 in bits 10 and 11 in the QA60 band were filtered out). Next, I made monthly composites of the single images to ensure complete images for the different glaciers. I tested different approaches to see which composites gave the best quality cloudless images, including composites based on the mean or median pixel value. Eventually, I rejected both this mean or median composite (combined with a lower than 40% cloud cover percentage) in favour of a so-called "quality composite". This is because this method provided visually much improved cloudless images. In the quality composite, I used Sentinel-2's "MSK_CLDPRB" band, which contains cloud probability, so that each pixel in the resulting mosaic received the values of the pixel with the lowest cloud probability among images.

Melt Pond Detection

The next step was to detect and classify melt ponds. I tested two approaches and compared them to see which provided the better result: a band ratio, or a random forest model.

Band Ratio

The first approach was adapted from Hochreuther et al. (2021). It entailed calculating a static band ratio between the blue and red band. My next step was to set a threshold, above which a pixel would be classified as 'pond', and given a value of 1; below was water, which was given a value of 0. I set this threshold by iteratively changing it, and manually verifying its correspondence to the true colour image. Using this approach, a threshold of 1.6 was determined to be the best. Following this, Hochreuter et al. applied multiple postprocessing steps to remove noise (e.g. (cloud) shadows) (2021). Due to the time constraints of this project, I decided to only apply the most influential postprocessing step applied in their paper. I determined this to be a sieve function that would filter out small random noise areas, which visually appeared to be the largest cause of error. For this, following their approach, I applied The Geospatial Data Abstraction Library (GDAL; an open-source geoprocessing tool providing raster and vector data models)'s gdal_sieve function (GDAL, n.d.).

Random Forest Model

Next, I tested a random forest (ML) method. First, this required taking a large composite image (see 'Preprocessing' above) and manually selecting training areas (i.e. pixels) in seven different classes: melt ponds, rock, greenery, open water, ice or snow, clouds, and cloud shadows. Subsequently, I could train a random forest model (creating 50 decision trees), after which I was able to apply the model to classify the entire image. This was an iterative process; after manual validation, it was at times necessary to go back to the training areas and add some more or adjust others, and train the model again. Finally, I saved the model to allow for classification of other images.

Manual Validation

Subsequently, I used manual validation to determine both algorithms' accuracy. This I did through manually selecting a handful of images from different months and regions, and visually comparing the true colour and classified images. Some images I selected randomly, and some were selected because they were outliers in further analysis (see paragraph "Pond Area" below).

Pond Area

This next step I applied for each different glacier I looked into in this study separately. To filter images based on glacier delineations, I used shapefiles adapted from Davies et al. (2020). Their paper presents a vast database of the geomorphology of Patagonia, which is provided for further use in their online supplementary data. This database contained a shapefile covering all glaciers in Southern America. I did some preprocessing in ArcGIS (version 3.3.0) to get to only

the data necessary for this study. First, I filtered the shapefile based on its "Region" field, to only be left with the glaciers in the SPI. Next, I made a separate shapefile of each glacier studied by filtering on the "GLAC_NAME" field.

Then, in this step, it was necessary to calculate the total melt pond area for any given image. I did this by classifying the image using the methods described above, and filtering the results so that only ponds were left (i.e. pond pixels were given values of 1, all other pixels were given a value of zero). Next, I could apply GEE's .pixelArea() function to find the area of each individual pond pixel. Finally, those individual pixels summed up left me with the total pond area. By looping through each image in the studied time period (December 2018 – December 2023; this was the period GEE had Sentinel-2 L2A data available for (ESA, n.d.-a)), and applying this workflow to every monthly composite image created, I was able to generate bar charts that show the variability in melt pond area over the months and years studied. Since melting exclusively occurs in summer, only the summer months (December – January – February (DJF) in the Southern Hemisphere) were included.

Besides these absolute value bar charts, I created the same charts using relative melt pond area. I did this in order to isolate the influence of total glacier area on melt pond area, and to better compare melting between glaciers without this area effect. Relative pond area was calculated using the total glacier areas listed in table 1.

Influence of the SAM

Subsequently, I performed a regression to find a possible association between pond area and the SAM. I tested only the SAM in this study, since the literature review suggested that this was the most influential mode both in this area and in the timespan studied. SAM data was taken from the USA National Oceanic and Atmospheric Administration (NOAA), who provide open access to their monthly averaged AAO (SAM) index data (NOAA, n.d.). I tested this regression in multiple different ways. First, I tested the monthly pond area against monthly SAM for all different glaciers separately. Additionally, I summed the pond area of all glaciers, and tested for correlation against monthly SAM. Lastly, I computed the seasonal mean values for both summed melt pond area and SAM and tested a regression between those. Both monthly per-glacier melt pond area and summed monthly and seasonal mean pond area were tested for correlation with SAM both without lag, and with a one-season lag. This is because there could be a time lag between SAM-influenced temperature change, and subsequent melting (i.e., SAM+ could have had a positive effect on spring temperatures, inducing increased melting in the subsequent summer).

Results

In Figure 5 we can see an example of a Sentinel-2 true colour image of a section of the SPI. It shows the end of a glacier that calves into a lake. Melt ponds can be seen, e.g. in the red circled area. Figure 6 shows the random forest classification of the image in Figure 5. Visual comparison of the classified band ratio and random forest results showed that on average, the random forest model performed better than the band ratio method. Therefore, it was decided to continue the analysis using the random forest model only. All subsequent data and figures will thus be based on the random forest model. Clearly, however, this model is not 100% accurate. See, for example, the on-glacier sediment in Figure 5 that is misclassified as being cloud shadows.

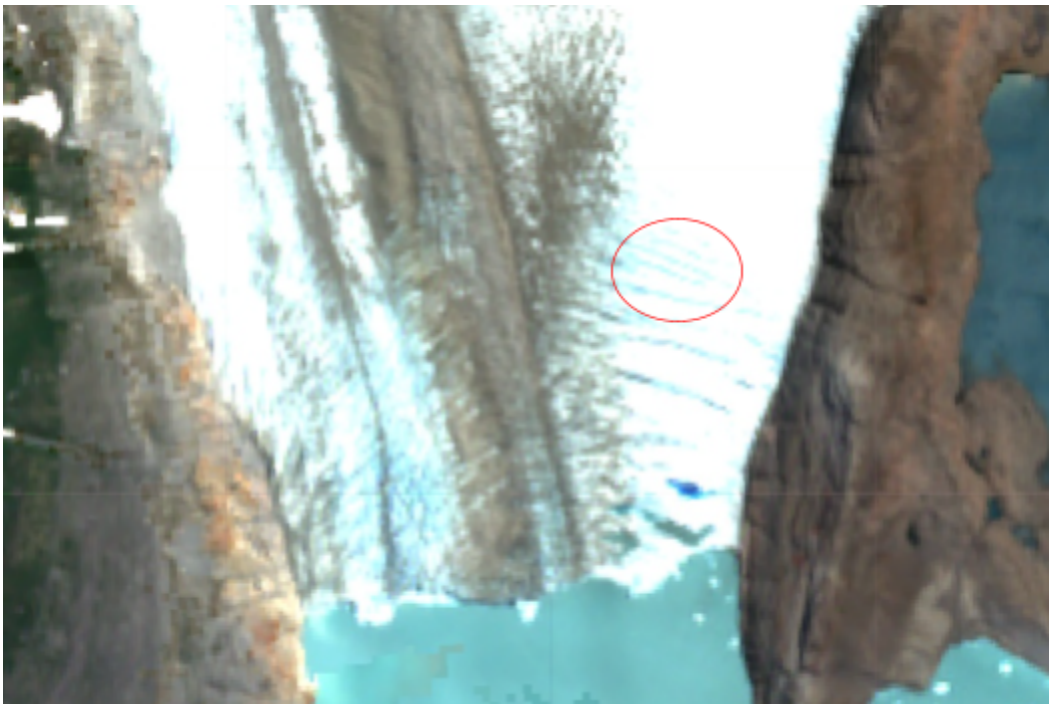

Figure 5: True colour zoomed-in section of the SPI, composite image of January 2023, Sentinel-2

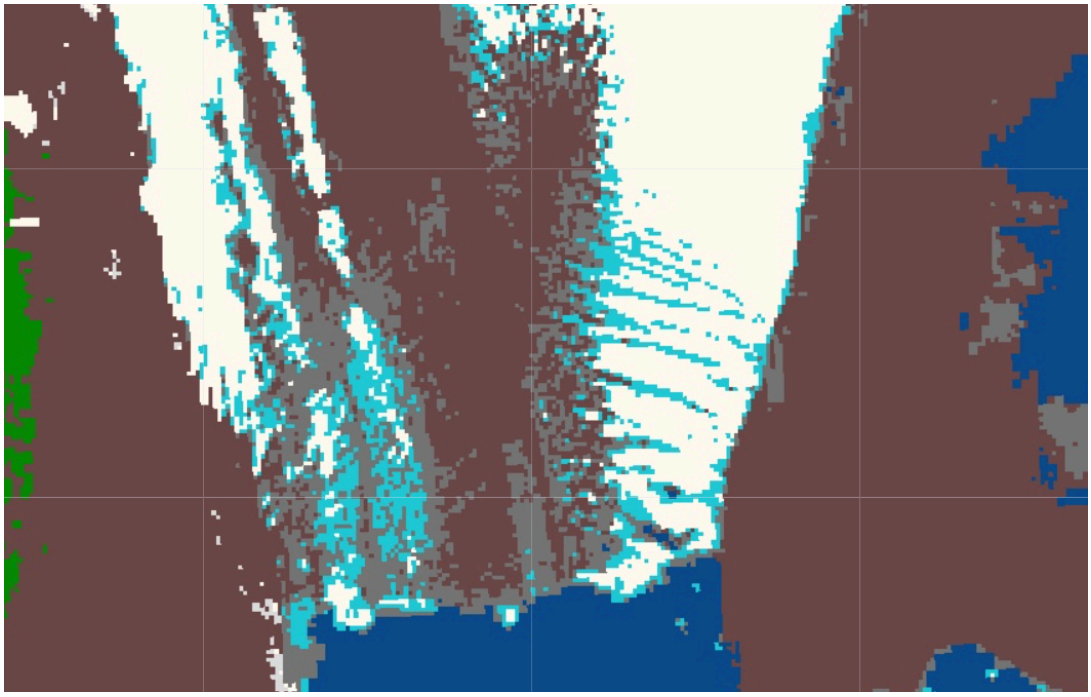

Figure 6: Random Forest Classification of the image of Figure 4 (January 2023), same area. Here, dark blue is open water; white is ice/snow; green is greenery; brown is rock; grey is cloud shadows; light blue is melt ponds.

Figures 7 to 14 are bar charts of the melt pond area in each summer month studied, per different glacier. As can be seen, there can be large inter-monthly and interannual variation for each glacier, as well as variability between glaciers. Due to the short timespan studied, no assumptions can be made about trends over time – the only inference possible to be made centres on variability within and between glaciers. Note that there are some bars missing: this denotes either cases where there was no sufficiently cloudless image available in the entire month – meaning there is no data on the melt ponds in this month – or cases where melt pond area was calculated to be zero km^2.

The same bar charts using calculated relative melt pond area instead of absolute area can be found in figures 15 to 22.

Generally, absolute pond area is highest on Upsala Glacier (Figure 12) and lowest on Chico (Figure 8). Where Upsala (figure 11) has seen melt pond areas of above 30 km^2, Chico's (Figure 7) maximum was closer to 4 km^2. Of course, total glacier area is a large explanatory factor here: Chico is the smallest glacier included in this study, where Upsala is one of the largest (see Table 1). Though, it is clear that area is not the only factor of influence. If it were, Pio XI (Figure 13) would have the largest melt pond area. Multiple outliers can be seen, where pond area is either close to zero (e.g. January 2023 on Jorge Montt, Figure 10) or higher than usual (e.g. February 2022 on Perito Moreno, Figure 7).

In contrast, comparing relative melt pond areas (Figures 15-22), these inter-glacier differences change. Upsala (Figure 20) and Chico (Figure 16) are now both among the glaciers

with the largest relative pond area (maxima around 3.5%; means of 1.9% and 1.7% respectively (Figure 23)). The smallest relative pond areas can be found on Pio XI (Figure 19) and O'Higgins (Figure 22), both with maxima of around 1% and means of 0.3% and 0.5% respectively (Figure 23).

Though there are outliers, for most glaciers it appears that February is the month with the highest pond area (Figures 7 to 14). Generally, in which months melting is highest and lowest is difficult to say, as it seems inconsistent: it varies between glaciers and over time. For example, February seems to be consistently the highest melt month on Perito Moreno (Figure 7), while this seems more mixed on e.g. O'Higgins (Figure 14). On Jorge Montt, the lowest melt month seems to be December (Figure 10), while this is less clear on Chico (Figure 8).

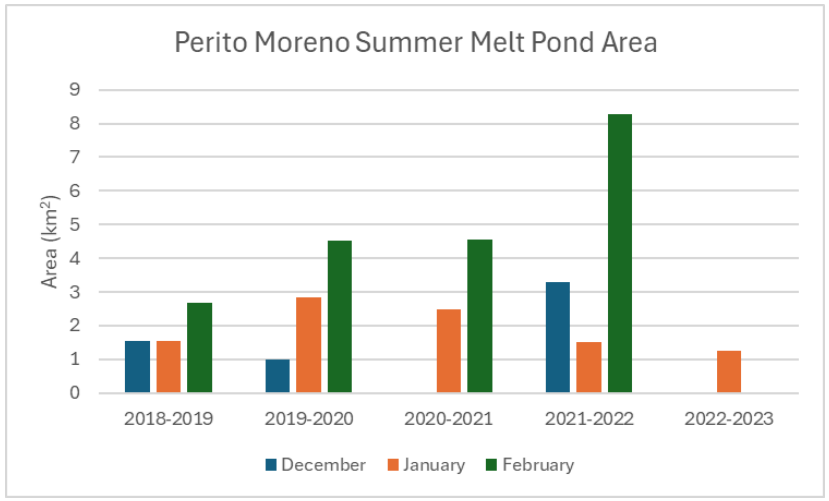

Figure 7: Monthly summer melt pond area on Perito Moreno glacier

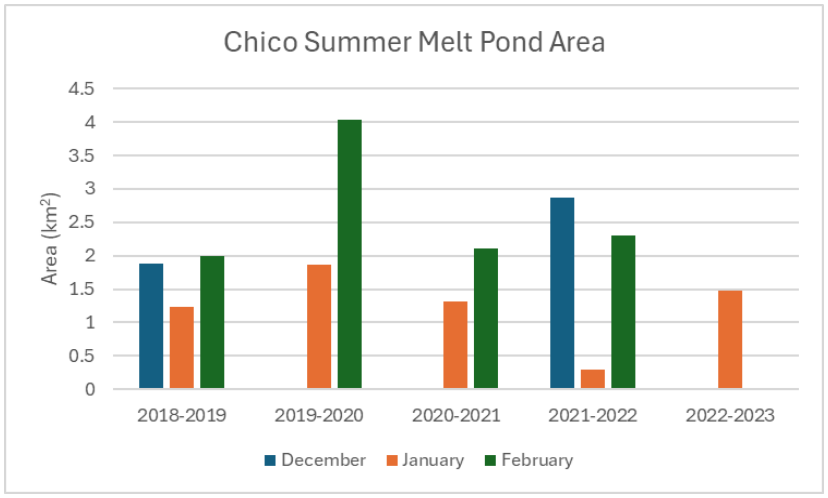

Figure 8: Monthly summer melt pond area on Chico glacier

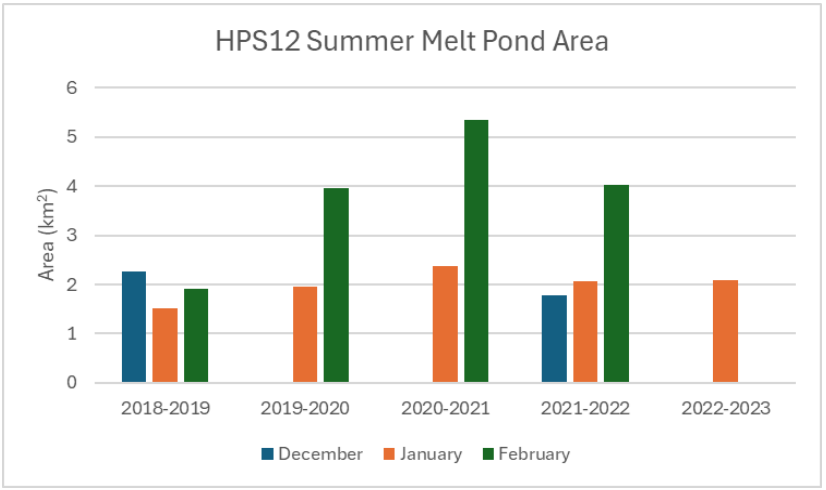

Figure 9: Monthly summer melt pond area on HPS12 glacier

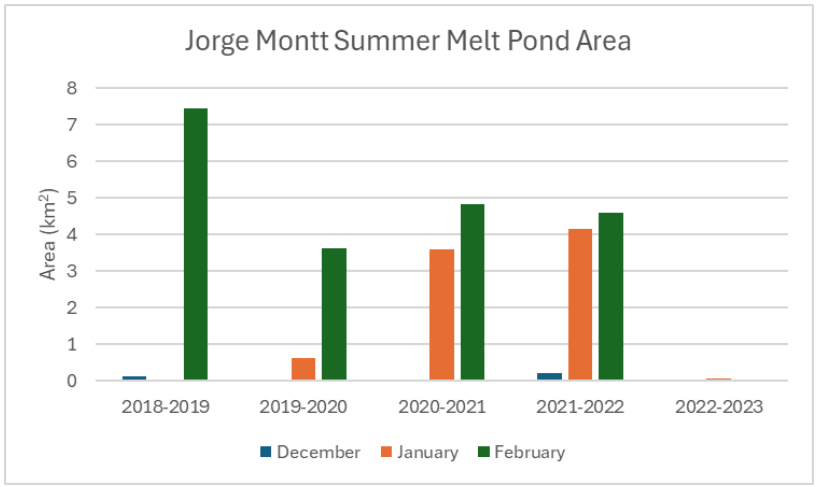

Figure 10: Monthly summer melt pond area on Jorge Montt glacier

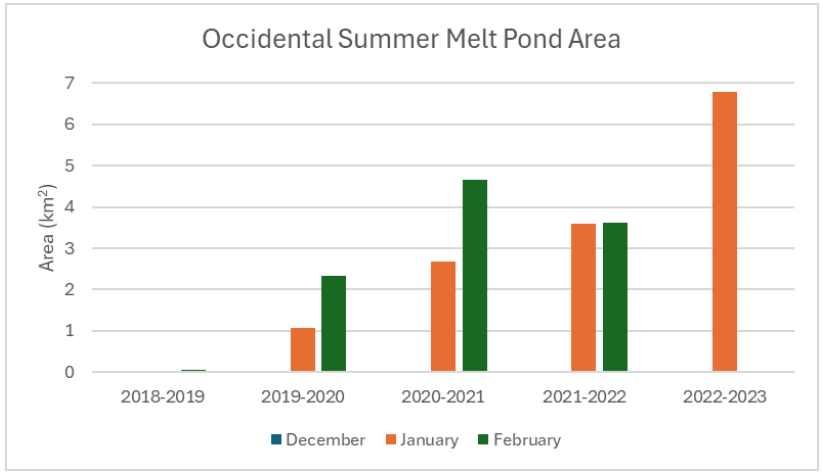

Figure 11: Monthly summer melt pond ara on Occidental glacier

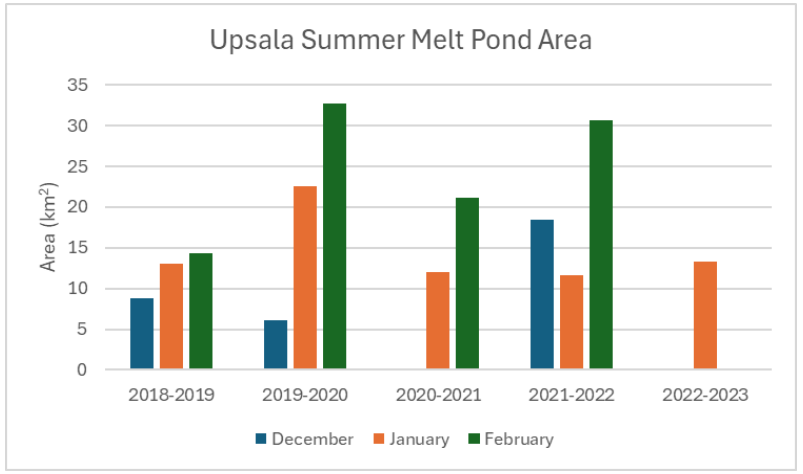

Figure 12: Monthly summer melt pond area on Upsala glacier

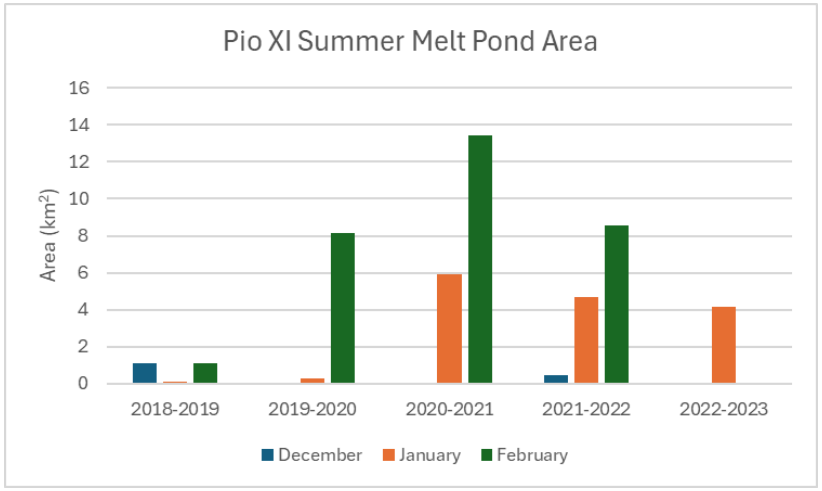

Figure 13: Monthly summer melt pond area on Pio XI glacier

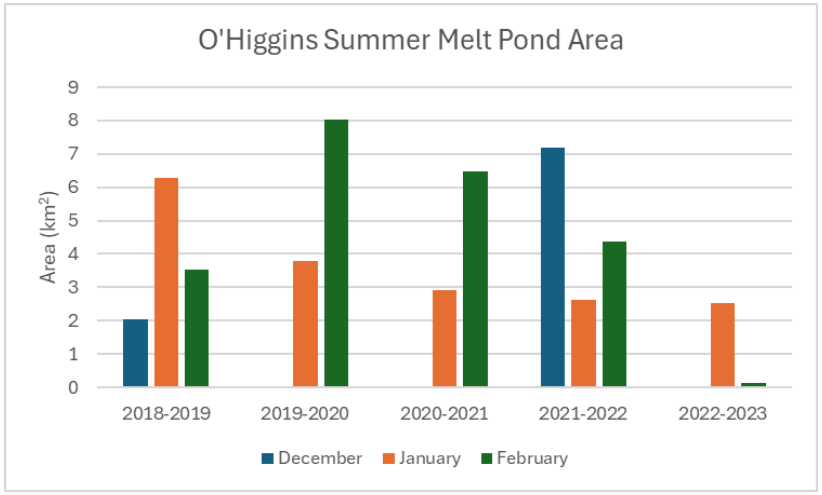

Figure 14: Monthly summer melt pond area on O'Higgins glacier

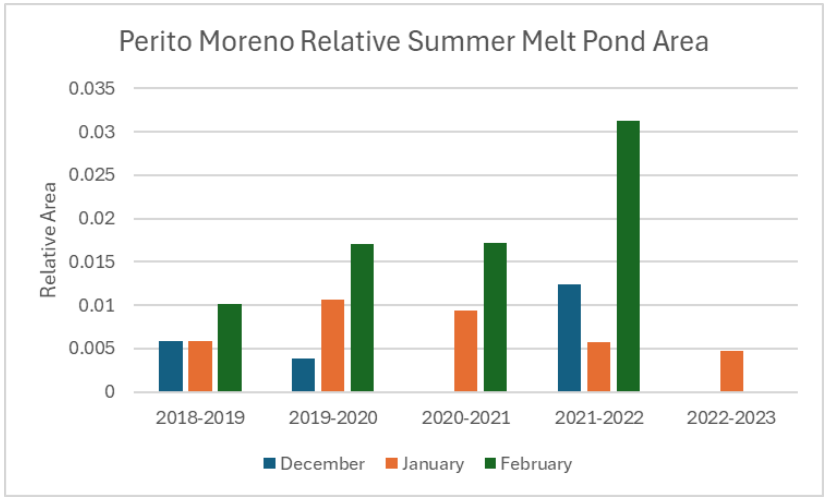

Figure 15: The same as Figure 6, but relative melt pond area

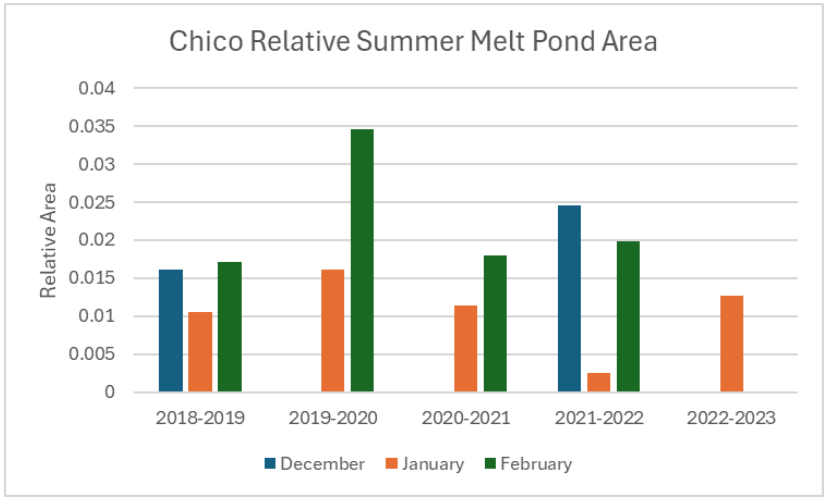

Figure 16: The same as Figure 7, but relative melt pond area

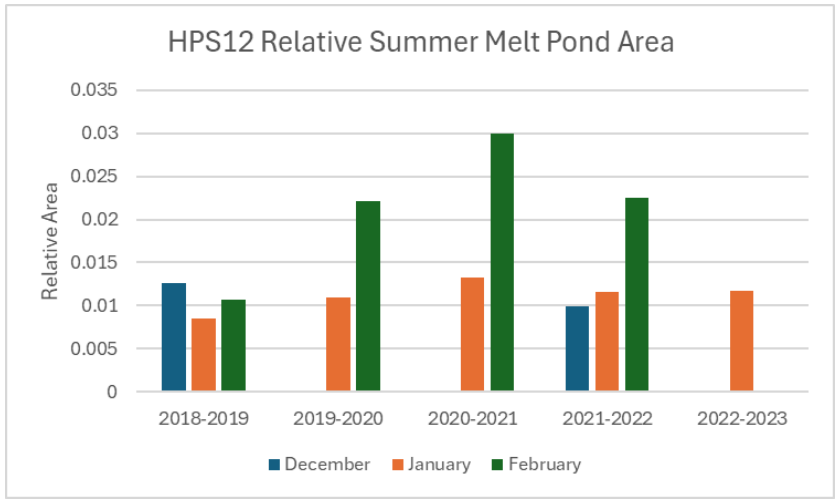

Figure 17: The same as Figure 8, but relative melt pond area

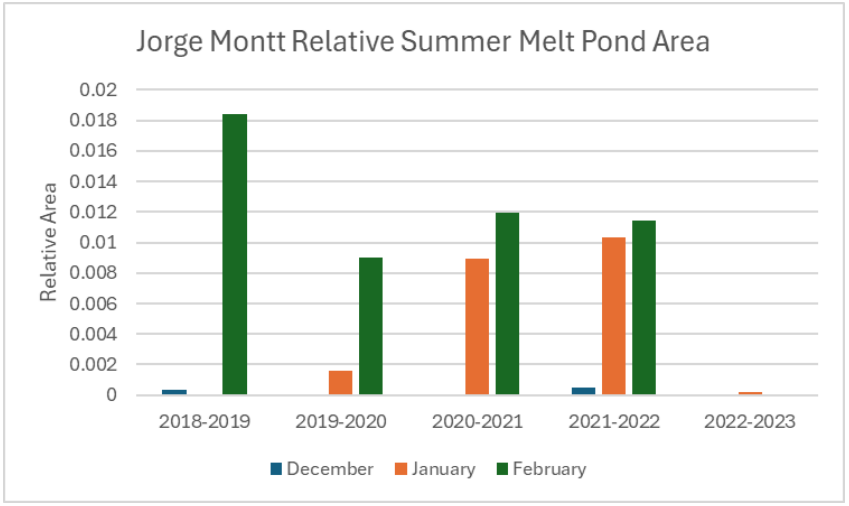

Figure 18: The same as Figure 9, but relative melt pond area

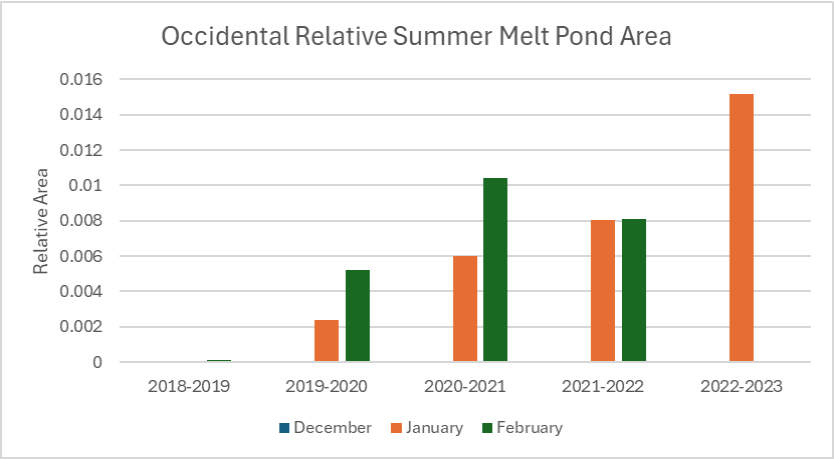

Figure 19: The same as Figure 10, but relative melt pond area

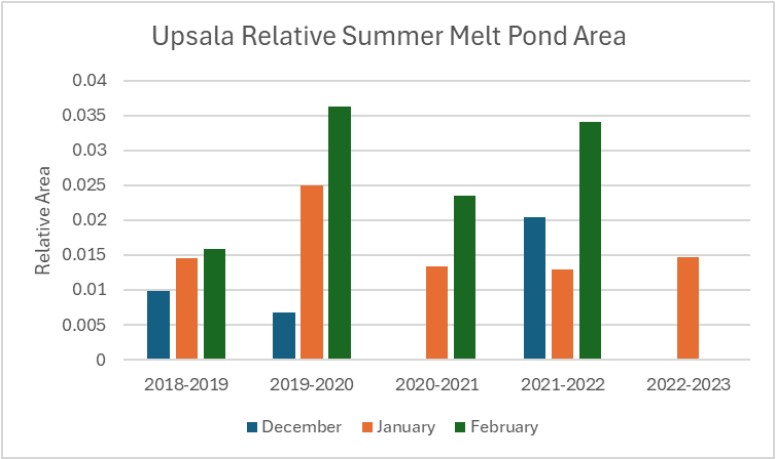

Figure 20: The same as Figure 11, but relative melt pond area

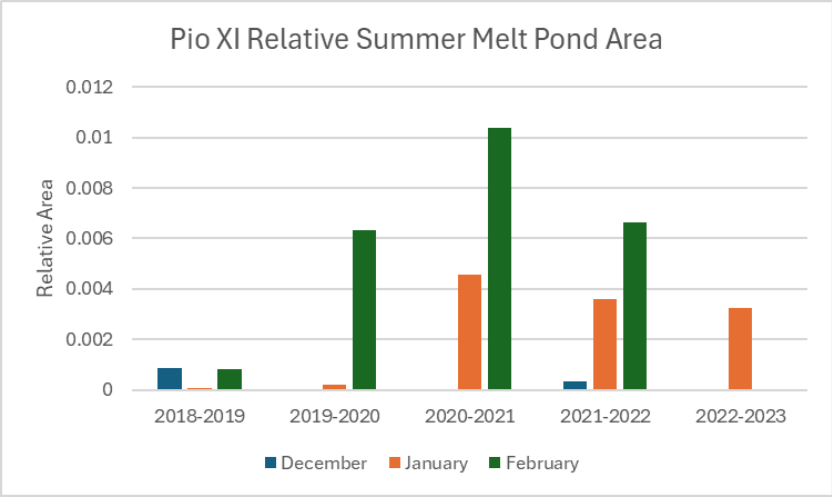

Figure 21: The same as Figure 12, but relative melt pond area

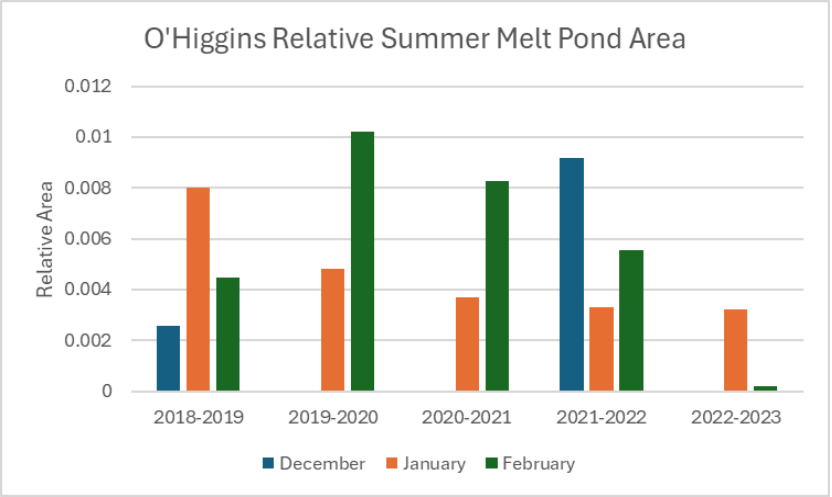

Figure 22: The same as Figure 13, but relative melt pond area

Figure 23 below shows the summer-averaged relative pond area per glacier studied. As can be seen, relative pond area varied from less than 0.5% to around 1.8% in this period. The highest relative pond areas were found on Upsala and Chico, while Pio XI and Occidental saw the lowest relative melting area.

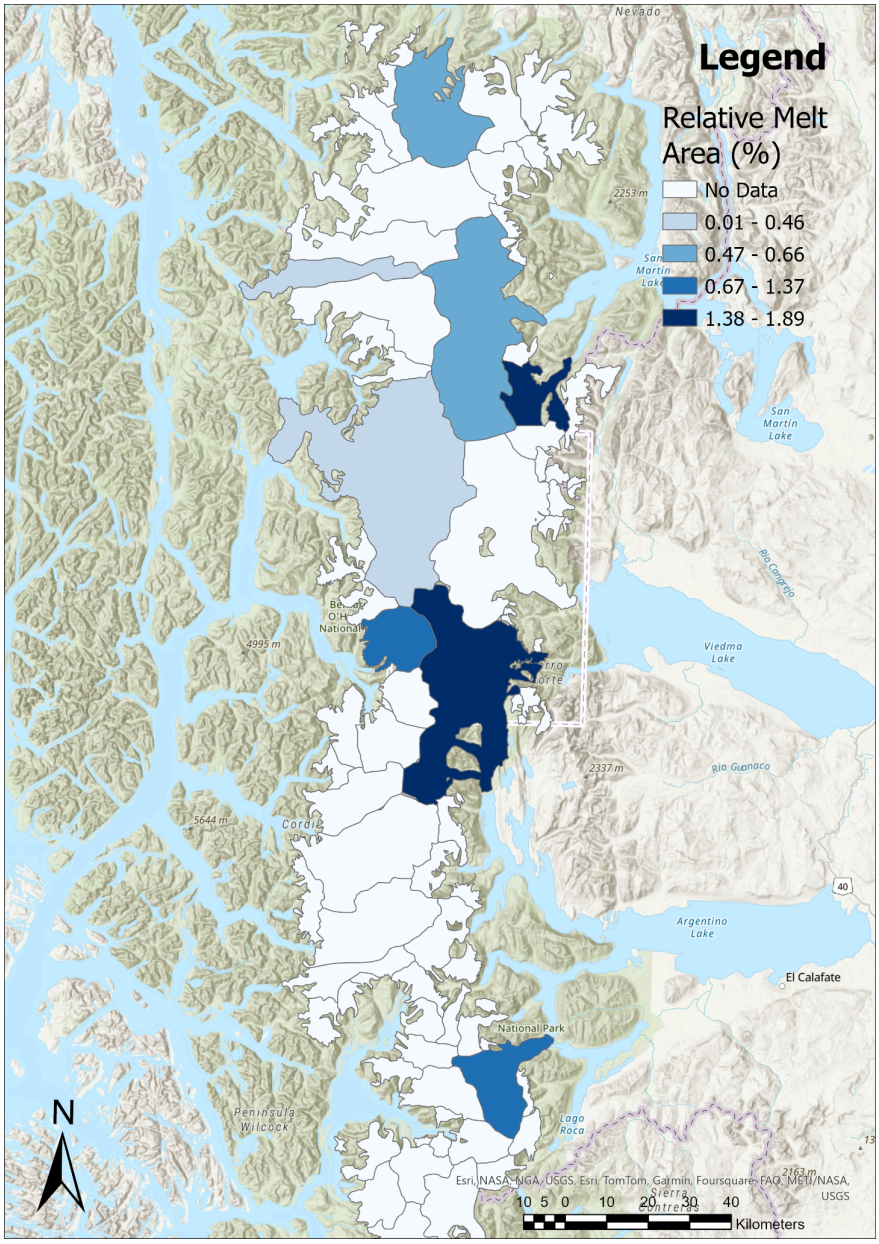

Figure 23: Average Summer Relative Melt Pond Area in % (2018-2023)

In Figure 24 we can see the same figure but instead using absolute pond area. As could be expected, this shows a different distribution, where Pio XI and Upsala have the highest area and Chico and Occidental the lowest.

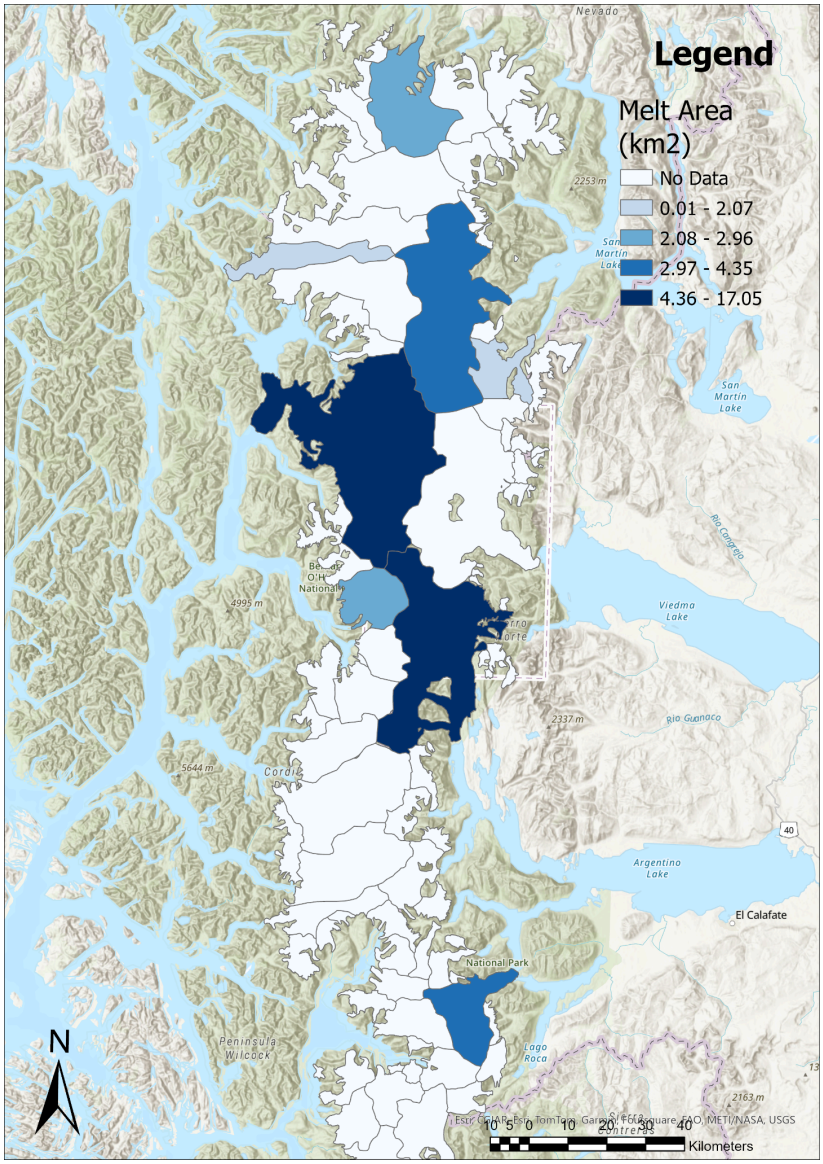

Figure 24: Average Summer Melt Pond Area in km² (2018-2023)

The next step in this study was to find a possible association between melt pond area and the SAM. Figures 25 and 26 below show the results of the pond area – SAM regression analysis without time lag, and with a one season time lag, respectively. From the wide spread of the data points, and the low R^2 values, it is clear that there is no correlation between the two in either case. This is the case as well in all other analyses performed (i.e. the per-glacier analyses, and the summed monthly: see SM1-10). Thus, it appears that SAM has no influence on melt pond area.

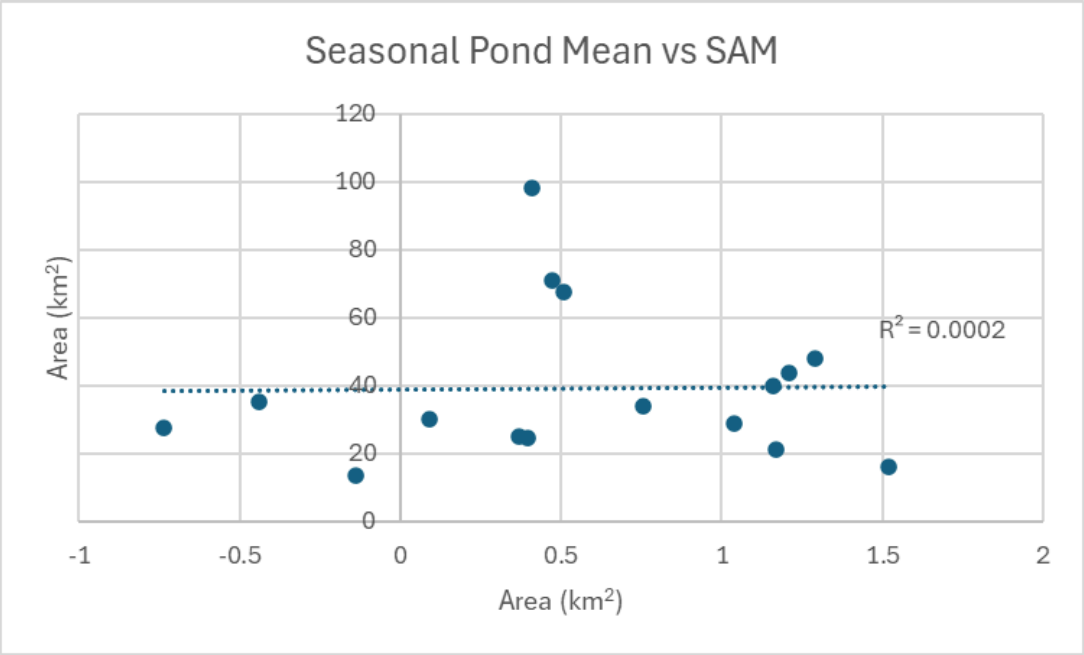

Figure 25: Correlation between SAM and total melt pond area summed over all 7 glaciers, both averaged per season

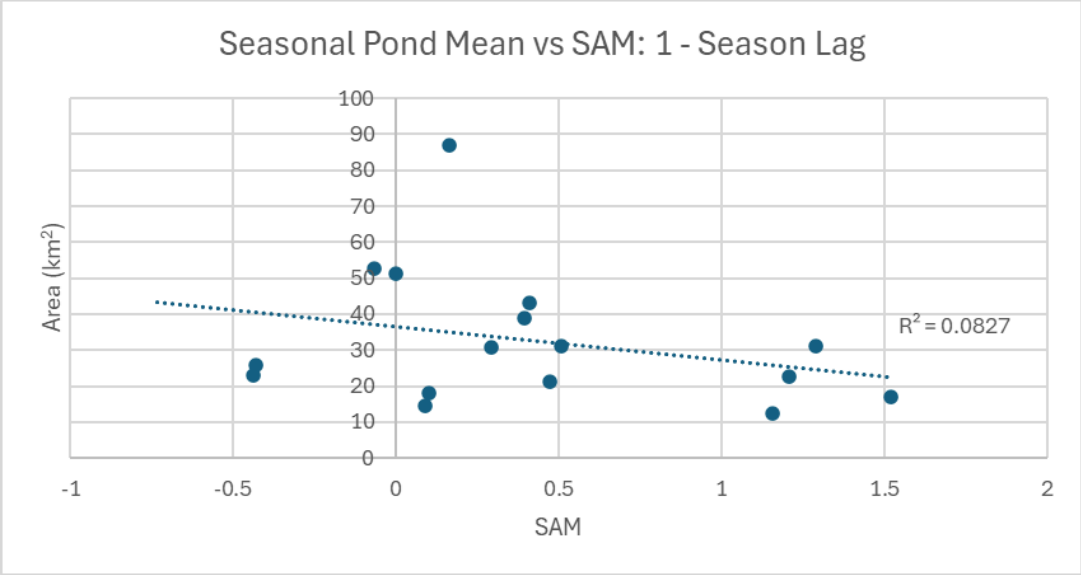

Figure 26: Correlation between SAM and total melt pond area summed over all 7 glaciers, both averaged per season, with a one-season time lag

Discussion

Inter-glacier Variability: Absolute and Relative Pond Area, East/West Divide

Especially Pio XI pond area seems to be consistent with previous findings (see Literature Review). Most studies agree that Pio XI is an outlier in the SPI, that has not been participating in the same general trend of thinning and retreat but even advanced (Foresta et al., 2018; López et al., 2010; Rignot et al., 2003). Indeed, my results show that although Pio XI has a high absolute melt area (Figures 13 and 24), its relative melt area is comparatively low (Figures 21 and 23). Results for Upsala seem consistent with previous findings as well. Similarly to my results (Figure 24), where Upsala had the highest melt pond area, Foresta et al. found the highest mass loss during their study period on this glacier as well (2018). Direct comparisons for the other glaciers are difficult to make, as most previous studies used some measure of total mass balance or elevation change that is not directly comparable to pond area (as mass balances take into account both melt and accumulation, and melt ponds are melt exclusively) (Foresta et al., 2018; López et al., 2010; Rignot et al., 2003).

Additionally, seasonality in pond area is difficult to characterise, as it seems inconsistent: Although February is the pond with the highest melt area, I found no month with a consistently lower pond area over time. This is contrary to results by Loriaux and Ruiz, who studied melt ponds on Verde Glacier in Chile between 2009 and 2019 (2021). They found a clear seasonality, where they saw a maximum in the amount of ponds in spring and the beginning of summer (i.e. November, December) and a minimum at the end of summer (i.e. March). This, according to them, can be explained by the annual evolution of the hydrological network. In spring and summer, this network is not yet well connected, so there are a large number of smaller ponds. These will later on increase in connectivity, reducing their total number. Some reasons why these results could differ is the fact that my study was limited to DJF only, focused on a different region, and the fact that Loriaux and Ruiz focused here on the number of ponds instead of the area (2021).

The East/West divide in climatic conditions of the SPI, caused by the orographic uplift on the ice field's western side, could be an explanatory variable of between-glacier variability as well. Of all studied glaciers, Pio XI, HPS12, Occidental, and O'Higgins are situated in the east of the SPI, and Perito Moreno, Chico, Upsala, and Jorge Montt are located in the west. Although this is not enough data to confirm for certain, Figure 23 does seem to agree with the hypothesis that there is a difference in melting between the east and west. In this period, relative melting appears to be higher on the eastern side of the ice field as compared to the western side. Although there are differences in our study areas, this is at odds with Bravo, Ross, et al.'s findings, who computed that from October 2015 to June 2016, ablation was higher in the west than in the east (2021). They describe observing a "glacier cooling effect" that is stronger in the east than in the west, ensuring they find less ablation in the east even though it gets more incoming shortwave radiation. Though, a drought during their study period ensured that melting in the west of the ice field was higher than normal – an effect that is of lower importance in my

study, considering Figures 23 and 24 are averaged over multiple years (Bravo, Ross, et al., 2021). This effect could at least partially explain the differences between our results.

In contrast, my results and those by Foresta et al. at least partially overlap (2018). They found the highest melting (measured by elevation change) in the north of the SPI, while in the south/southwest elevation remained more stable in the period from April 2011 to March 2017. My results are consistent with theirs in the sense that both Foresta et al. and I found the highest melting occurring on Upsala glacier, and the lowest (or even an elevation gain, in their case) on Pio XI. In my results, however, the north-south divide is less clear, though this can be at least partially explained by the fact that I have less data available: while they studied the SPI as a whole, I have glacier-averaged results for a few set glaciers. They write that north-south differences in elevation are the reason behind the north-south divide in melt behaviour: a greater proportion of ice in the north is situated at lower elevations (Foresta et al., 2018).

Intra-glacier Variability: the SAM

Besides the observed between-glacier variability in melt pond area, Figures 7-14 show variability over time as well for each glacier separately. My study looked into the SAM as a possible explanatory factor: some results of this regression analysis are shown in Figures 24 and 25. There appears not to be an association between SAM and melt pond area. This is interesting, as previous research indicated that the SAM has a significant influence over (South) Patagonian surface air temperature, and that melting is responsive to temperature and temperature changes. However, this does agree with Carrasco-Escaff et al.'s results: they found poor correspondence between surface mass balance and SAM (2023). They found that SAM+ causes a simultaneous strengthening of the westerlies over the Patagonian icefields and a warming of Patagonia, and that SAM- causes a weakening of the westerlies as well as a cooling over Patagonia. This, they write, ensures that both effects on surface mass balance "cancel each other out", ensuring that there is no net effect of SAM on surface mass balance (Carrasco-Escaff et al., 2023).

Limitations and Recommendations for Future Research

This study had some important limitations, that would benefit from being addressed in future research. Firstly, the short timespan and the cloudy nature of the area resulted in there being a low number of images available for further analysis. Additionally, the no-data months decreased the reliability of the analysis, especially of the calculations of seasonal averages. Further research should be conducted utilising data from different satellite products (e.g. MODIS). Whereas the limitation of this satellite is that its data is much more spatially coarse, and thus might capture melt ponds with much lower accuracy than Sentinel-2 can, it has daily data over a much larger range of time than Sentinel-2 was available for. This both ensures that there will be more sufficiently cloudless images available for each month, and the ponds can be studied over a much longer period.

Secondly, in this study I looked into seven out of the total of 48 glaciers in the SPI. This makes the data difficult to generalise for the entire ice field. Future studies could consider

applying the analysis to more, or different glaciers in the SPI, or even adding the NPI as well. It would be interesting to gain a more complete overview of the whole area's melting, and to make comparisons between the two ice fields.

Another important limitation was put forward by Dell et al. (2024). They looked into meltwater on Antarctic ice shelves, and write that this meltwater is either stored in ponds (as this study looked into) or as "slush": saturated firn or snow. Slush is an important factor influencing melt dynamics. To name a few processes, it can be a precursor of melt ponds, if snow/firn pore spaces are filled with meltwater more quickly than can be drained away. When it refreezes, it can form impermeable ice lenses that facilitates the formation of melt ponds in subsequent years. Similarly to melt ponds, it can incentivise further melting through the positive melt – albedo feedback. Dell et al. applied a random forest ML model to Landsat 8 images of Antarctic ice shelves during the austral summers (November–March) of 2013–2021, and found that during this period melt ponds and slush had roughly equal areas (2024). Thus, they write that studies that do not take into account slush, like the present one, might significantly underestimate the total melt area. Future research would benefit from taking this limitation into account, and adding a slush class to the random forest classification (though this comes with difficulties of its own, as slush is very spectrally similar to other classes, such as melt ponds, snow, and blue ice) (Dell et al., 2024).

Moreover, further research would benefit from more manual validation of the images' classifications. Due to the time constraints of the present study, I was unable to look into all outlier images. For example, some images returned a melt pond area of exactly 0. The results of this study could have been increased in reliability by manually looking into these outlier images, and updating the model if deemed necessary. Furthermore, reliability of results could have been improved by applying a different method of validation. This could be, for example, the "expert elicitation" that Dell et al. apply in their study, where they ask a number of glaciology experts to manually verify a set of pixels (2021). It might also be helpful to compare the result of two different (e.g. machine learning) model classifications.

On that note, I recommend future research to apply different machine learning methods than the random forest that the present study was built on. One example could be convolutional neural networks (CNN). This is a type of ML model that utilises layers of several filters to extract features from images (Damiani et al., 2024). Recently, CNNs are increasingly applied to climate: for example, Damiani et al. applied CNN to downscale four meteorological variables (mean temperature, solar surface radiation, wind speed, and precipitation) and found that it outperformed other linear and nonlinear methods tested (2024). CNNs could have a significant potential for the study of melt ponds as well, since they take into account not only the band reflectance values of each pixel separately, but pond shape as well.

Furthermore, in this study I looked into only a limited number of explanatory factors. I tested the SAM for correlation with melt ponds, and I briefly discussed total glacier area, east/west location, and seasonality. Of course, there are many more factors that can be worth looking into. To provide some examples, more climate modes could be tested for associations:

these could include ENSO, and the ANINO. The latter mode might especially prove significant, as prior research showed that there is an association between the ANINO and extreme temperatures (see Literature Review).

In addition, a factor of interest was put forward by Carrasco-Escaff et al.: the Drake Passage (2023). This is a passage connecting the southern Atlantic and Pacific Oceans, between the southern part of South America and the Antarctic South Shetland Islands (see Figure 3). Carrasco-Escaff et al. found associations between the Drake Low (an anomalous low-pressure zone over the Drake Passage, leading to circulation changes and enhanced westerlies that lead to increased precipitation) and a positive mass balance of the Patagonian Ice Fields, and between the opposite conditions and a lower surface mass balance (2023). It would be interesting to look into whether this Drake Low has an influence on melt pond area as well as on precipitation-induced changes in total mass balance.

Besides climate modes and circulation-influencing factors, it would be interesting to look into climate variables as additional explanatory factors of melt variability. These could include air temperature and precipitation.

Lastly, since this analysis was done on a per-glacier basis, it was not possible to look into possible associations between melt area and altitude. It would have been too much of a generalisation to use each glacier's average altitude. Instead, it would be interesting to combine classified melt pond images with a Digital Elevation Map (DEM) to find whether melt varies over different elevation levels.

Conclusion

In this study, I looked into the variability in melt pond area in seven glaciers in the Southern Patagonian Icefield in 2018-2023. The research question of this study was: "How can the SPI glaciers' melt ponds be characterised, and what influence does the SAM have over their occurrence?"

Firstly, a main finding of this study is that there is a large variability in pond area between different glaciers: relative pond area varied from a mean of 0.3% to 1.9%. The glaciers with the largest relative pond area were Upsala and Chico, while the smallest relative areas could be found on Pio XI and O'Higgins. These findings are partially consistent with previous findings by Foresta et. al (2018).

Second, there is a clear variability over time that appears inconsistent: though February appeared to be the month with the highest overall pond area, my results showed no seasonality in pond area that was consistent for all glaciers studied. Over time melt pond area varied from 0% to 3.5%.

On the variability in pond area, the SAM appeared to have no significant effect. This was the case for all relationships tested: e.g. both for all glaciers separately and summed up, and both when comparing with and without a time lag.

Overall, it appears that there are factors at play other than the ones I looked into in this study, that influence the melting behaviour of the SPI's glaciers.

References

Aravena, J., & Luckman, B. H. (2008). Spatio‐temporal rainfall patterns in Southern South America. *International Journal of Climatology*, *29*(14), 2106–2120. https://doi.org/10.1002/joc.1761

Bamber, J. L., Westaway, R. M., Marzeion, B., & Wouters, B. (2018). The land ice contribution to sea level during the satellite era. *Environmental Research Letters*, *13*(6), 063008. https://doi.org/10.1088/1748-9326/aac2f0

Braun, M. H., Malz, P., Sommer, C., Farías-Barahona, D., Sauter, T., Casassa, G., Soruco, A., Skvarca, P., & Seehaus, T. C. (2019). Constraining glacier elevation and mass changes in South America. *Nature Climate Change*, *9*(2), 130–136. https://doi.org/10.1038/s41558-018-0375-7

Bravo, C., Bozkurt, D., Ross, A., & Quincey, D. J. (2021). Projected increases in surface melt and ice loss for the Northern and Southern Patagonian Icefields. *Scientific Reports*, *11*(1). https://doi.org/10.1038/s41598-021-95725-w

Bravo, C., Quincey, D. J., Ross, A. N., Rivera, A., Brock, B., Miles, E., & Silva, A. (2019). Air temperature characteristics, distribution, and impact on modeled ablation for the South Patagonia Icefield. *Journal of Geophysical Research. Atmospheres*, *124*(2), 907–925. https://doi.org/10.1029/2018jd028857

Bravo, C., Ross, A. N., Quincey, D. J., Cisternas, S., & Rivera, A. (2021). Surface ablation and its drivers along a west–east transect of the Southern Patagonia Icefield. *Journal of Glaciology/Journal of Glaciology*, *68*(268), 305–318. https://doi.org/10.1017/jog.2021.92

Carrasco-Escaff, T., Rojas, M., Garreaud, R. D., Bozkurt, D., & Schaefer, M. (2023). Climatic control of the surface mass balance of the Patagonian Icefields. ˜*the œCryosphere*, *17*(3), 1127–1149. https://doi.org/10.5194/tc-17-1127-2023

Carrivick, J. L., Davies, B. J., James, W. H., Quincey, D. J., & Glasser, N. F. (2016). Distributed ice thickness and glacier volume in southern South America. *Global and Planetary Change*, *146*, 122–132. https://doi.org/10.1016/j.gloplacha.2016.09.010

Casassa, G., Rivera, A., Aniya, M., & Naruse, R. (2002). Current knowledge of the Southern Patagonia Icefield. In *Series of the Centro de Estudios Científicos de Santiago* (pp. 67–83). https://doi.org/10.1007/978-1-4615-0645-4_7

Cazenave, A., & Llovel, W. (2010). Contemporary sea level rise. *Annual Review of Marine Science*, *2*(1), 145–173. https://doi.org/10.1146/annurev-marine-120308-081105

Damiani, A., Ishizaki, N. N., Sasaki, H., Feron, S., & Cordero, R. R. (2024). Exploring super-resolution spatial downscaling of several meteorological variables and potential applications for photovoltaic power. *Scientific Reports*, *14*(1). https://doi.org/10.1038/s41598-024-57759-8

Davies, B. J., Darvill, C. M., Lovell, H., Bendle, J. M., Dowdeswell, J. A., Fabel, D., García, J. L., Geiger, A., Glasser, N. F., Gheorghiu, D. M., Harrison, S., Hein, A. S., Kaplan, M. R., Martin, J. R., Mendelova, M., Palmer, A., Pelto, M., Rodés, Á., Sagredo, E. A., . . . Thorndycraft, V. R. (2020). The evolution of the Patagonian Ice Sheet from 35 ka to the

present day (PATICE). *Earth-science Reviews*, *204*, 103152. https://doi.org/10.1016/j.earscirev.2020.103152

Dell, R. L., Banwell, A. F., Willis, I. C., Arnold, N. S., Halberstadt, A. R. W., Chudley, T. R., & Pritchard, H. D. (2021). Supervised classification of slush and ponded water on Antarctic ice shelves using Landsat 8 imagery. *Journal of Glaciology/Journal of Glaciology*, *68*(268), 401–414. https://doi.org/10.1017/jog.2021.114

Dell, R. L., Willis, I. C., Arnold, N. S., Banwell, A. F., & De Roda Husman, S. (2024). Substantial contribution of slush to meltwater area across Antarctic ice shelves. *Nature Geoscience*. https://doi.org/10.1038/s41561-024-01466-6

Donat-Magnin, M., Jourdain, N. C., Gallée, H., Amory, C., Kittel, C., Fettweis, X., Wille, J. D., Favier, V., Drira, A., & Agosta, C. (2020). Interannual variability of summer surface mass balance and surface melting in the Amundsen sector, West Antarctica. ˜*the* œ*Cryosphere*, *14*(1), 229–249. https://doi.org/10.5194/tc-14-229-2020

Dussaillant, I., Berthier, É., Brun, F., Masiokas, M., Hugonnet, R., Favier, V., Rabatel, A., Pitte, P., & Ruiz, L. (2019). Two decades of glacier mass loss along the Andes. *Nature Geoscience*, *12*(10), 802–808. https://doi.org/10.1038/s41561-019-0432-5

ESA. (n.d.-a). *Copernicus Sentinel-2 Collection-1 Availability Status*. Sentinel Online. https://sentinels.copernicus.eu/en/web/sentinel/technical-guides/sentinel-2-msi/copernicus-sentinel-2-collection-1-availability-status

ESA. (n.d.-b). *Satellite constellation*. The European Space Agency. Retrieved July 5, 2024, from https://www.esa.int/Applications/Observing_the_Earth/Copernicus/Sentinel-2/Satellite_constellation

ESA. (2016, April 11). *Pío XI Glacier, Chile*. The European Space Agency. Retrieved February 11, 2024, from https://www.esa.int/ESA_Multimedia/Images/2016/11/Pio_XI_Glacier_Chile

Foresta, L., Gourmelen, N., Weissgerber, F., Nienow, P., Williams, J., Shepherd, A., Drinkwater, & Plummer, S. (2018). Heterogeneous and rapid ice loss over the Patagonian Ice Fields revealed by CryoSat-2 swath radar altimetry. *Remote Sensing of Environment*, *211*, 441–455. https://doi.org/10.1016/j.rse.2018.03.041

Garreaud, R. D., Vuille, M., Compagnucci, R., & Marengo, J. (2009). Present-day South American climate. *Palaeogeography, Palaeoclimatology, Palaeoecology*, *281*(3–4), 180–195. https://doi.org/10.1016/j.palaeo.2007.10.032

Garreaud, R., Lopez, P., Minvielle, M., & Rojas, M. (2013). Large-Scale control on the Patagonian climate. *Journal of Climate*, *26*(1), 215–230. https://doi.org/10.1175/jcli-d-12-00001.1

GDAL. (n.d.). *gdal_sieve — GDAL documentation*. GDAL Documentation. Retrieved July 8, 2024, from https://gdal.org/programs/gdal_sieve.html

Google Earth Engine. (n.d.-a). *Harmonized Sentinel-2 MSI: MultiSpectral Instrument, Level-2A*. Earth Engine Data Catalog. Retrieved July 5, 2024, from

https://developers.google.com/earth-engine/datasets/catalog/COPERNICUS_S2_SR_HARMONIZED

Google Earth Engine. (n.d.-b). *Supervised Classification*. Retrieved July 8, 2024, from https://developers.google.com/earth-engine/guides/classification

Google Earth Engine. (n.d.-c). *Unsupervised Classification (clustering)*. Retrieved July 8, 2024, from https://developers.google.com/earth-engine/guides/clustering

Hata, S., & Sugiyama, S. (2021). Changes in the Ice-Front position and surface elevation of glaciar Pío XI, an advancing calving glacier in the southern Patagonia Icefield, from 2000–2018. *Frontiers in Earth Science*, *8*. https://doi.org/10.3389/feart.2020.576044

Hochreuther, P., Neckel, N., Reimann, N., Humbert, A., & Braun, M. (2021). Fully automated detection of supraglacial lake area for Northeast Greenland using Sentinel-2 Time-Series. *Remote Sensing*, *13*(2), 205. https://doi.org/10.3390/rs13020205

Loikith, P. C., Detzer, J., Mechoso, C. R., Lee, H., & Barkhordarian, A. (2017). The influence of recurrent modes of climate variability on the occurrence of monthly temperature extremes over South America. *Journal of Geophysical Research. Atmospheres*, *122*(19). https://doi.org/10.1002/2017jd027561

López, P., Chevallier, P., Favier, V., Pouyaud, B., Ordenes, F., & Oerlemans, J. (2010). A regional view of fluctuations in glacier length in southern South America. *Global and Planetary Change*, *71*(1–2), 85–108. https://doi.org/10.1016/j.gloplacha.2009.12.009

Loriaux, T., & Ruiz, L. (2021). Spatio-Temporal distribution of Supra-Glacial ponds and ice cliffs on Verde Glacier, Chile. *Frontiers in Earth Science*, *9*. https://doi.org/10.3389/feart.2021.681071

Malz, P., Meier, W., Casassa, G., Jaña, R., Skvarca, P., & Braun, M. (2018). Elevation and Mass Changes of the Southern Patagonia Icefield Derived from TanDEM-X and SRTM Data. *Remote Sensing*, *10*(2), 188. https://doi.org/10.3390/rs10020188

NOAA. (n.d.). *Antarctic Oscillation (AAO)*. National Weather Service | Climate Prediction Center. Retrieved July 8, 2024, from https://www.cpc.ncep.noaa.gov/products/precip/CWlink/daily_ao_index/aao/aao.shtml

Pasquini, A. I., & Depetris, P. J. (2011). Southern Patagonia's Perito Moreno Glacier, Lake Argentino, and Santa Cruz River hydrological system: An overview. *Journal of Hydrology*, *405*(1–2), 48–56. https://doi.org/10.1016/j.jhydrol.2011.05.009

Phiri, D., Simwanda, M., Salekin, S., Nyirenda, V., Murayama, Y., & Ranagalage, M. (2020). Sentinel-2 Data for Land Cover/Use Mapping: A Review. *Remote Sensing*, *12*(14), 2291. https://doi.org/10.3390/rs12142291

Rignot, E., Rivera, A., & Casassa, G. (2003). Contribution of the Patagonia icefields of South America to sea level rise. *Science*, *302*(5644), 434–437. https://doi.org/10.1126/science.1087393

Schaefer, M., Machguth, H., Falvey, M., Casassa, G., & Rignot, E. (2015). Quantifying mass balance processes on the Southern Patagonia Icefield. *The Cryosphere*, *9*(1), 25–35. https://doi.org/10.5194/tc-9-25-2015

Tamiminia, H., Salehi, B., Mahdianpari, M., Quackenbush, L., Adeli, S., & Brisco, B. (2020). Google Earth Engine for geo-big data applications: A meta-analysis and systematic review. *ISPRS Journal of Photogrammetry and Remote Sensing*, *164*, 152–170. https://doi.org/10.1016/j.isprsjprs.2020.04.001

Willis, M. J., Melkonian, A. K., Pritchard, M. E., & Rivera, A. (2012). Ice loss from the Southern Patagonian Ice Field, South America, between 2000 and 2012. *Geophysical Research Letters*, *39*(17). https://doi.org/10.1029/2012gl053136

Supplementary Materials

Random Forest Pond Classification Code

```
// Cloud masking function
var maskS2clouds = function(img) {
  var qa = img.select('QA60');
  var cloudBitMask = 1 << 10;
  var cirrusBitMask = 1 << 11;
  var mask = qa.bitwiseAnd(cloudBitMask).eq(0)
  .and(qa.bitwiseAnd(cirrusBitMask).eq(0)
  );
  return img.updateMask(mask).divide(10000);
};


// Mosaic using pixel quality method
var dataset_qual = ee.ImageCollection('COPERNICUS/S2_SR_HARMONIZED')
                .filterDate('2023-12-01', '2023-12-31')
                .filterBounds(perito_moreno)
                .filter(ee.Filter.lt('CLOUDY_PIXEL_PERCENTAGE', 30))
                .map(maskS2clouds);

print(dataset_qual); // to see number of images

dataset_qual = dataset_qual.map(function(img){
  var cloudProb = img.select('MSK_CLDPRB');
  var cloudProbInv = cloudProb.multiply(-1).rename('quality');
  return img.addBands(cloudProbInv);
});

var img = dataset_qual.qualityMosaic('quality');

// Merge all training areas
var gcps =
ponds.merge(rock).merge(greenery).merge(open_water).merge(ice_snow).merge(clouds).merge(
cloud_shadows);

// Overlay the point on the image to get training data.
var training = img.sampleRegions({
```

```
  collection: gcps,
  properties: ['surface_area'],
  scale: 10
});

// Train a classifier.
var classifier = ee.Classifier.smileRandomForest(50).train({
  features: training,
  classProperty: 'surface_area',
  inputProperties: img.bandNames()
});

// Using the random forest classifier defined earlier, export the random
// forest classifier as an Earth Engine asset.
var classifierMeltPondDetection =
'projects/ee-thesis-lauri-glaciers/assets/sentinel2_random_forest_improved';
Export.classifier.toAsset(
  classifier,
  'Saved-random-forest-pond-classification',
  classifierMeltPondDetection
);

// Classify rest of image
var classified = img.classify(classifier);

// Add classified and true colour image to map
var palette = ['#1fc9d6', '#6c4747', '#078b05', '#0b4a8b', '#fffaef', '#dcdcdc', '#757575'];

Map.addLayer(classified, {min: 0, max: 6, palette: palette}, 'Sentinel RF');

Map.addLayer(img, vis_params, 'Best-pixel mosaic (by cloud score)');
```

Melt Pond Area Code

```
// change glacier import up above to run analysis for different ROI

// function for clipping glacier area
var clipToCol = function(img) {
  return img.clip(glacier);
};

// function to mask out clouds
var maskS2clouds = function(img) {
  var qa = img.select('QA60');

  var cloudBitMask = 1 << 10;
  var cirrusBitMask = 1 << 11;

  var mask = qa.bitwiseAnd(cloudBitMask).eq(0)
  .and(qa.bitwiseAnd(cirrusBitMask).eq(0)
  );

  return img.updateMask(mask).divide(10000);
};

// inverse cloud probability
var invCloudProb = function(img) {
    var cloudProb = img.select('MSK_CLDPRB');
    var cloudProbInv = cloudProb.multiply(-1).rename('quality');
    return img.addBands(cloudProbInv);
};

// load saved model
var savedClassifier =
ee.Classifier.load('projects/ee-thesis-lauri-glaciers/assets/sentinel2_random_forest_improved');

// function to classify model
var classify = function(img) {
  var classified = img.classify(savedClassifier);
  return classified.copyProperties(img, ['fileName','system:time_start', 'system:time_end']);
};
```

```
var startDate = '2015-07-01';
var endDate = '2024-05-31';

// function to get monthly median composite
var getMonthlyComposite = function(year, month) {
  var startDate = ee.Date.fromYMD(year, month, 1);
  var endDate = startDate.advance(1, 'month');
  var data = ee.ImageCollection('COPERNICUS/S2_SR_HARMONIZED')
    .filterBounds(glacier)
    .filterDate(startDate, endDate)
    .filter(ee.Filter.lt('CLOUDY_PIXEL_PERCENTAGE', 30))
    //.filter(ee.Filter.listContains('system:band_names', 'B1'))
    .map(maskS2clouds)
    .map(clipToCol)
    .map(invCloudProb)
    .qualityMosaic('quality')
    .set('system:time_start', startDate.millis())
    .set('system:time_end', endDate.millis())
    .set('fileName', ee.String('monthly_clasification_').cat(startDate.format('YYYY-MM')));

  return data;
};

// empty image collection to store monthly composite
var monthlyComposite = ee.ImageCollection([]);

// loop over months and apply function above to each month, then append result to image
collection
for (var year = 2015; year <= 2023; year++) {
  var months = [9, 10, 11, 12, 1, 2, 3];
  for (var i in months) {
    var data = getMonthlyComposite(year,months[i]);
    var temporaryCollection = ee.ImageCollection([data]); // temp collection with single image in
iteration
    monthlyComposite = monthlyComposite.merge(temporaryCollection);
  }
}

// filter out empty images where there wasn't a good image all month
```

```
var monthlyCompositeNoNull =
monthlyComposite.filter(ee.Filter.listContains('system:band_names', 'B1'));

// classify all images using function defined above
var monthlyClassification = monthlyCompositeNoNull.map(classify);

// area calculation of whole glacier
var glacier_area = glacier.geometry().area();
var glacier_area_sqkm = ee.Number(glacier_area).divide(1e6);
print(glacier_area_sqkm);

// function to calculate pond area: gives each pond pixel the value of its area, else 0
var pondArea = function(classified_img) {
  var ponds = classified_img.eq(0);

  var area_ponds = ponds.multiply(ee.Image.pixelArea());

  // area_ponds = area_ponds.copyProperties(classified_img, ['fileName','system:time_start',
'system:time_end']);

  var date = classified_img.get('system:time_start');
  var area = area_ponds.reduceRegion({
    reducer: ee.Reducer.sum(),
    geometry: glacier,
    scale: 10,
    maxPixels: 1e14
  });

  return ee.Feature(null, {area: area.get('classification'), 'system:time_start': date});
};

// apply function above to image collection
var pondArea = monthlyClassification.map(pondArea);

print(pondArea);

print(ui.Chart.feature.byFeature(pondArea.sort('system:time_start'), 'system:time_start', 'area'));
```

SAM Regressions

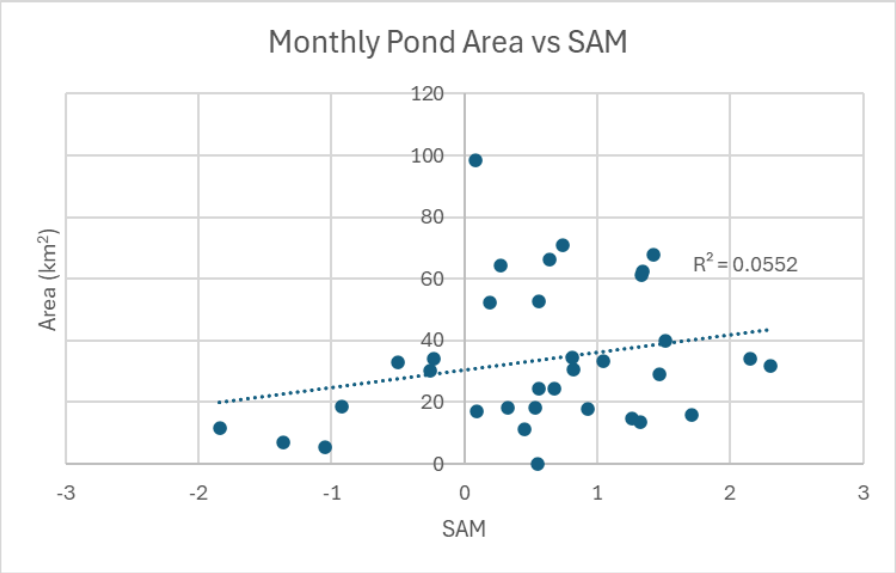

Figure SM1: Monthly summed pond area against SAM

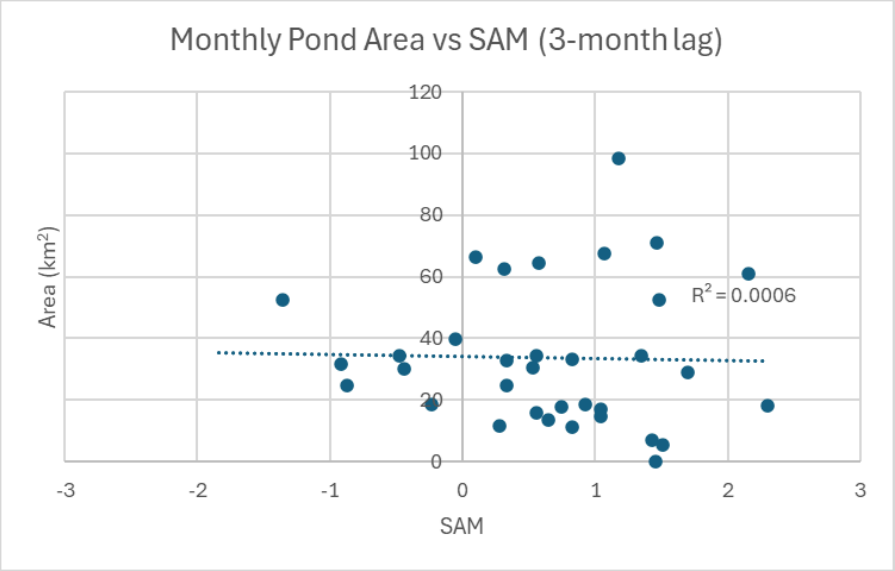

Figure SM2: The same as figure SM1, with a 3-month time lag

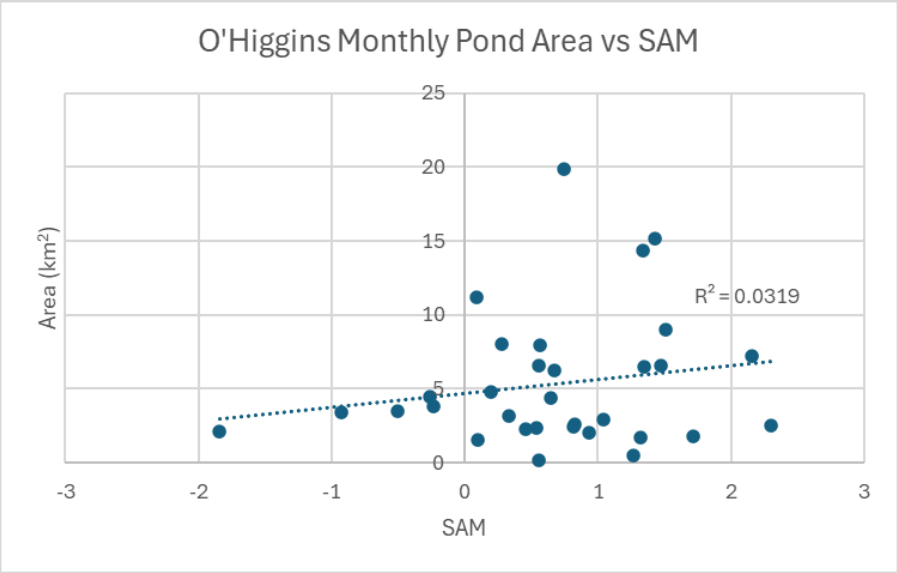

Figure SM3: Monthly pond area vs SAM on O'Higgins

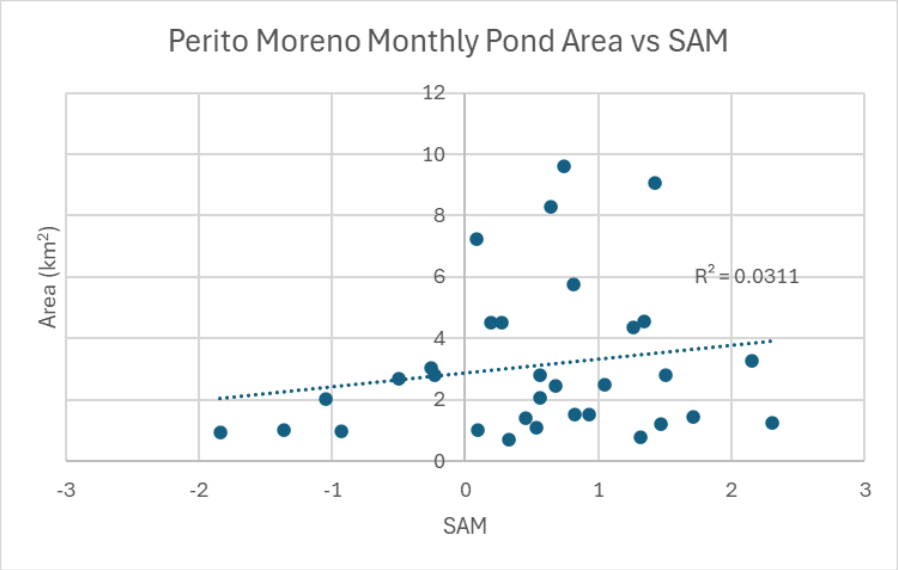

Figure SM4: Monthly Pond Area vs SAM on Perito Moreno

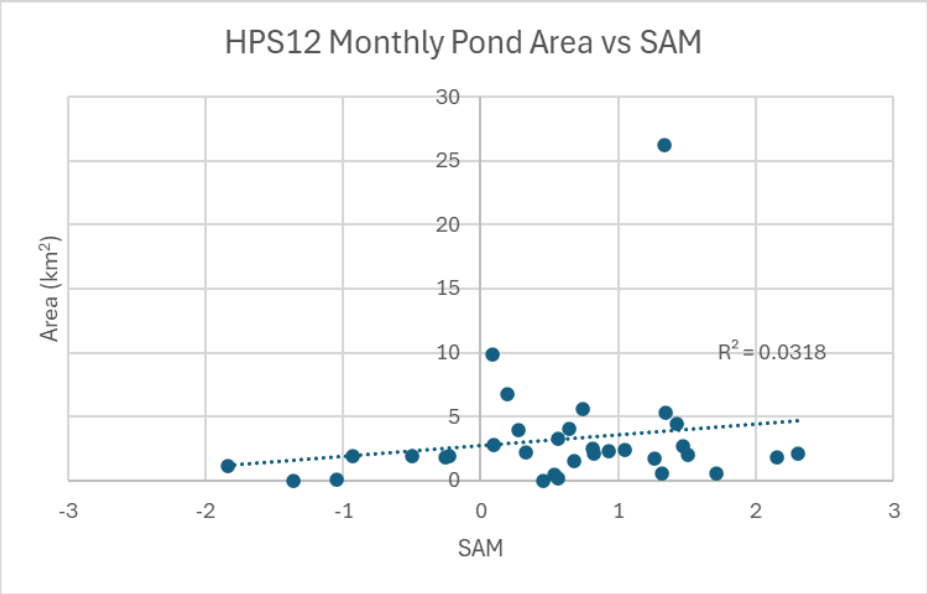

Figure SM5: Monthly Pond Area vs SAM on HPS12

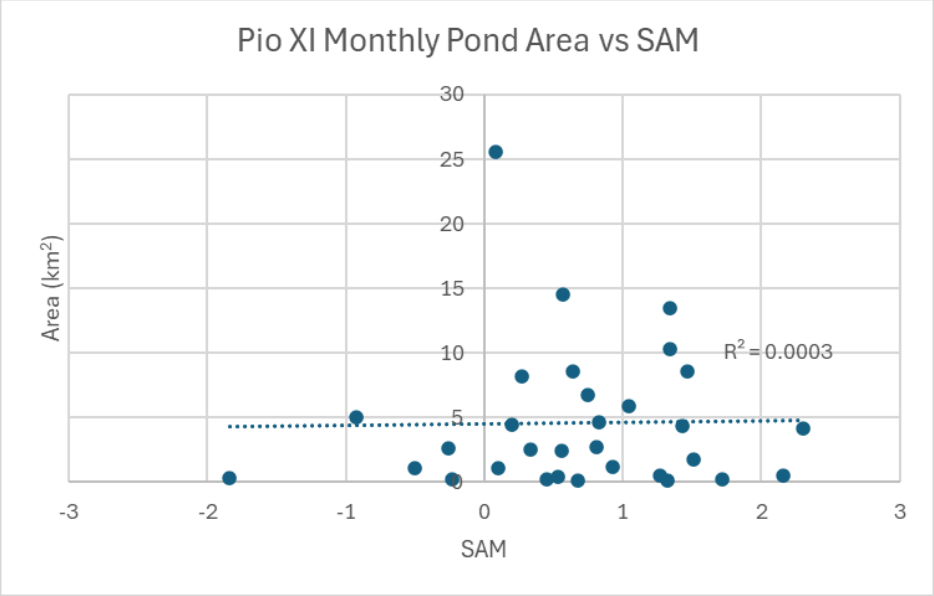

Figure SM6: Monthly Pond Area vs SAM on Pio XI

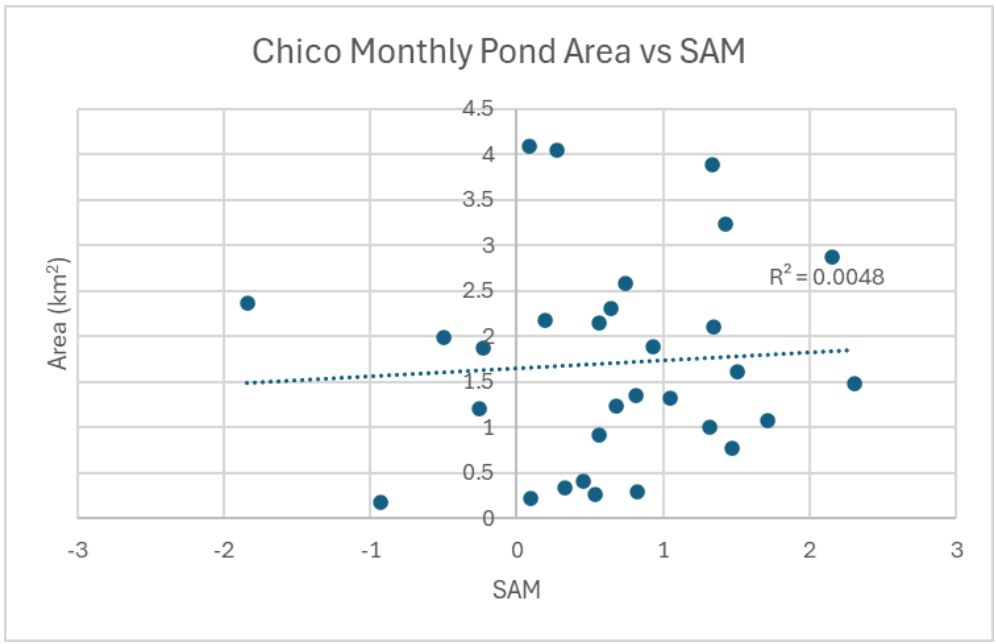

Figure SM7: Monthly Pond Area vs SAM on Chico

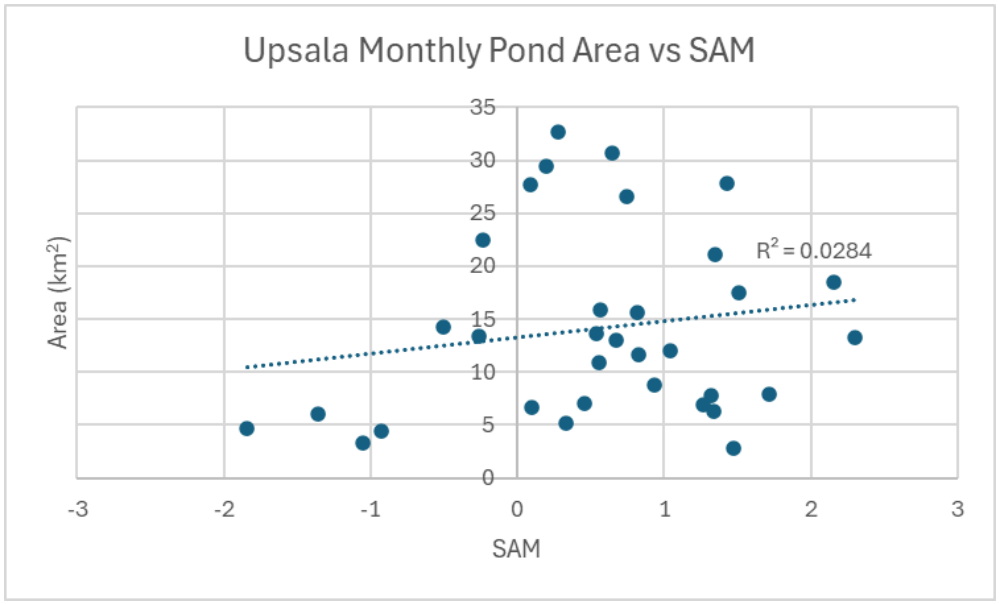

Figure SM8: Monthly Pond Area vs SAM on Upsala

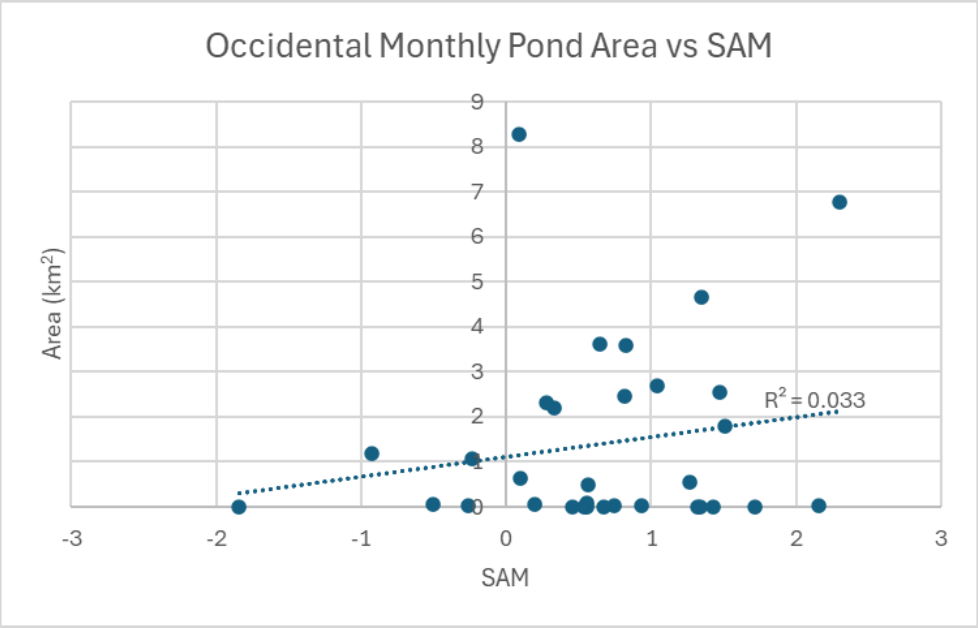

Figure SM9: Monthly Pond Area vs SAM on Occidental

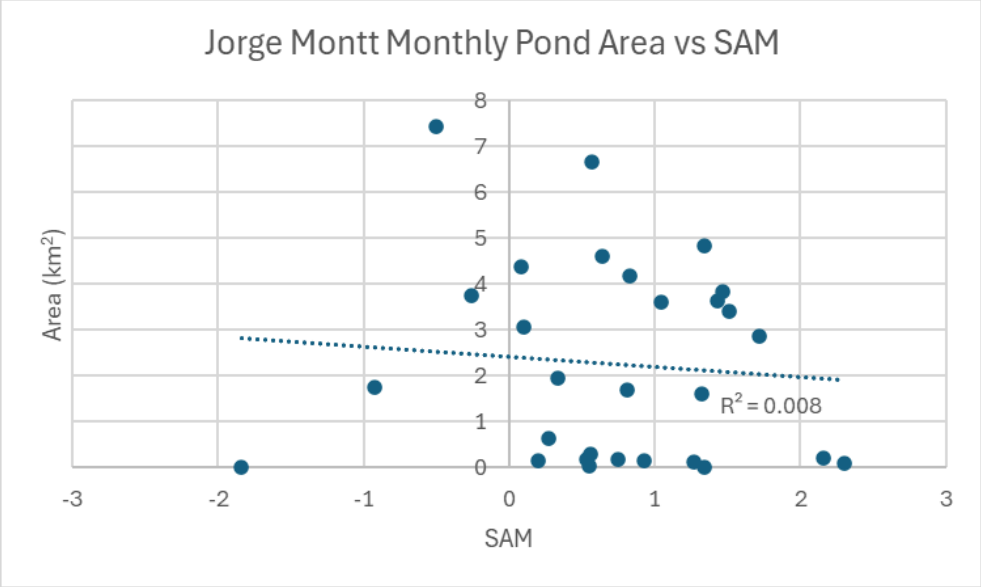

Figure SM10: Monthly Pond Area vs SAM on Jorge Montt